Chapter 14
Pulsed Laser Ablation of Soft Biological Tissues

Alfred Vogel and Vasan Venugopalan

14.1 Introduction

In this chapter we focus on the key elements that form our current understanding of the mechanisms of pulsed laser ablation of soft biological tissues. We present a conceptual framework providing mechanistic links between various ablation applications and the underlying thermodynamic and phase change processes [1]. We define pulsed laser ablation as the use of laser pulses with duration of $\sim$1 ms or less for the incision or removal of tissue regardless of the photophysical or photochemical processes involved. However, we will confine this presentation to pulsed ablation performed on a tissue level that does not involve laser-induced plasma formation. Ablation processes within transparent tissues or cells resulting from nonlinear absorption have been considered in reviews by Vogel and Venugopalan [1] and by Vogel and co-workers [2].

14.2 Tissue Properties Relevant for Ablation

Although early consideration of laser ablation treated tissue with properties equivalent to water, it soon became apparent that *tissue composition*, as well as its optical, thermal, and mechanical properties, play important roles on both the ablation dynamics and outcome. Soft biological tissues consist of cells that reside in and attach to an extracellular matrix (ECM). By mass, the composition of most soft tissues is dominated by water (55–99%) and collagen (0–35%). In "cell-continuous" tissue such as liver and epithelia, the ECM fraction is quite small and consists mostly of cell adhesion proteins. By contrast, "matrix-continuous tissues" that include the corneal stroma, dermis, cartilage, and tendon have a very small cellular fraction and are almost entirely ECM. In matrix-continuous tissues (see Fig. 14.1), the ECM consists largely of collagen, with the collagen content being as high as 35% [1, 3–5].

A. Vogel (✉)
Institute of Biomedical Optics, University of Lübeck, Lübeck, Germany
e-mail: vogel@bmo.uni-luebeck.de

A.J. Welch, M.J.C. van Gemert (eds.), *Optical-Thermal Response of Laser-Irradiated Tissue*, 2nd ed., DOI 10.1007/978-90-481-8831-4_14,

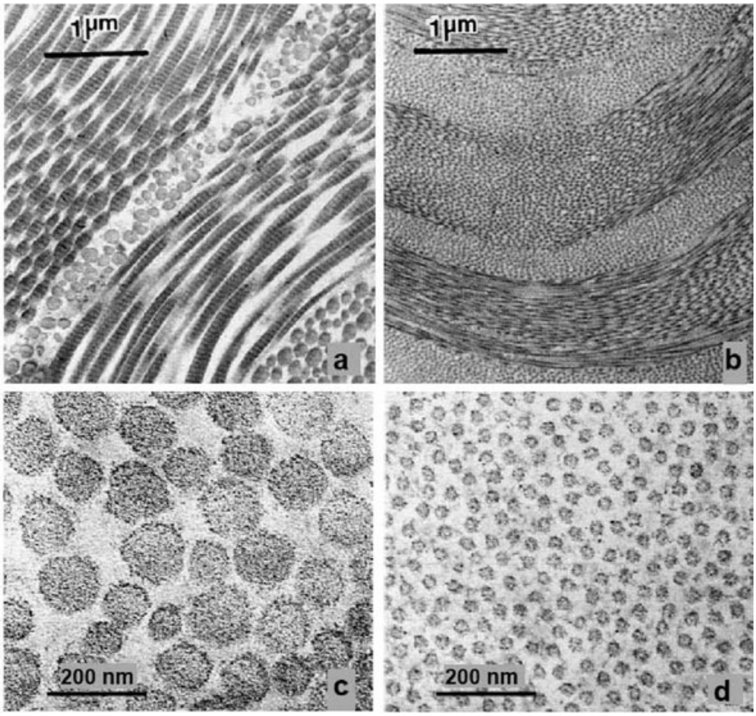

Fig. 14.1 Transmission electron micrographs of the sclera (**a**, **c**) and corneal stroma (**b**, **d**) showing an arrangement of collagen fibrils that are embedded in a ground substance with high water content. (Reprinted with permission from [6])

Nearly all the water content resides in the ground substance between the collagen fibrils [1, 7]. The primary ECM function is the maintenance of the tissue's structural integrity. As a result, the ECM inhibits both tissue vaporization and material removal that represent the desired outcomes of ablation processes.

Figure 14.2a summarizes the absorption spectra of proteins, melanin, hemoglobin, and water that govern the deposition of the incident laser energy in pulsed laser ablation. A more detailed discussion of the *optical absorption properties* of tissues is presented in Chapter 3 and Ref. [1]. In non-turbid samples, optical transmission is governed by Beer-Lambert's law, and the amount of deposited laser energy decays exponentially with depth. In the absence of scattering, the reciprocal of the absorption coefficient $\mu_a[\mathrm{cm}^{-1}]$ defines the optical penetration depth δ [cm], i.e. $\delta = (1/\mu_a)$, and thus the characteristic depth of laser energy deposition.

For most laser wavelengths used only a single tissue constituent (e.g., water or collagen) absorbs the radiation; thus macroscopic energy deposition is inhomogeneous. Heat diffusion tends to level out these inhomogeneities, and the extent to which this occurs during the ablation process depends both on the spatial scale that characterize the distribution of these constituents and the laser pulse duration

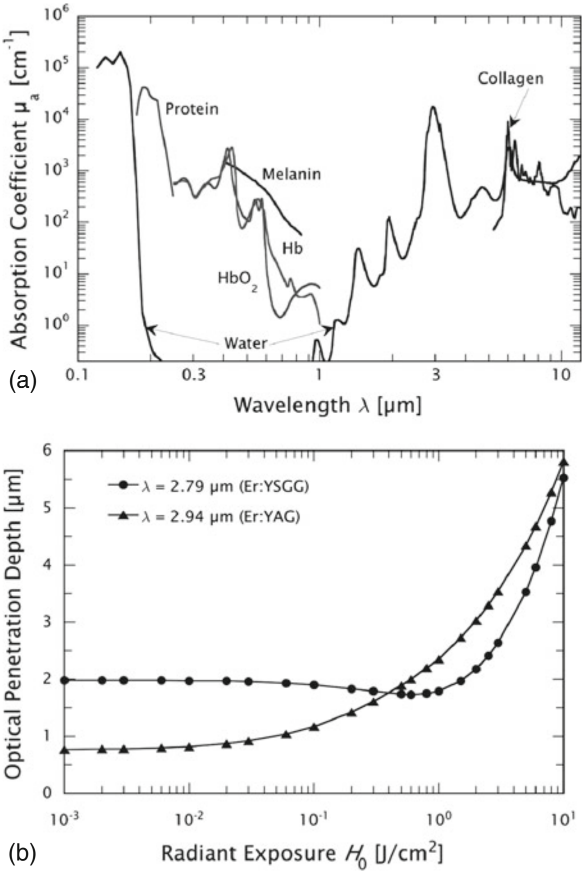

Fig. 14.2 Optical properties relevant for ablation. (**a**) Optical absorption coefficients of principal tissue chromophores in the 0.1–12 μm spectral region. (**b**) Variation of optical penetration depth of water with incident radiant exposure for Er:YAG ($\lambda = 2.94\,\mu$m) and Er:YSGG ($\lambda = 2.79\,\mu$m) laser irradiation. (Reprinted with permission from [1])

(see Section 14.3). An important spatial scale characterizing domains with different absorption properties is given by the diameter and spacing of the collagen fibrils because most tissue water resides in either cells or in the ground substance of the ECM between the collagen fibrils. The fibril diameter is ≈30 nm in cornea and varies between 20 nm and 120 nm in dermis. The center-to-center spacing is very regular (≈65 nm) in the transparent cornea and exhibits more variations in other tissues [1, 3, 7].

Optical scattering arises from spatial variations in refractive index within tissue that are particularly strong between collagen fibrils and ground substance. Typical reduced scattering coefficients for tissues in the visible spectral region are on the order of $\mu'_s = 10 - 40\,\mathrm{cm}^{-1}$ [1, 8]. Optical scattering will reduce the optical penetration depth, δ, of light relative to the absorption depth, $(1/\mu_a)$. In addition, when scattering is dominant over absorption, backscattering and total internal reflection lead to a fluence rate close to the tissue surface that can exceed by several times the incident irradiance [9]. Moreover, the peak fluence can be reached below the surface. However, ablation is typically performed at wavelengths where $\mu_a >> \mu'_s$.

Precise tissue ablation is achieved using laser wavelengths that exhibit very large absorption coefficients (Fig. 14.2a), such as the radiation of ArF excimer lasers ($\lambda = 193$ nm), Er:YSSG lasers ($\lambda = 2.79\,\mu$m), Er:YAG lasers ($\lambda = 2.94\,\mu$m) lasers ($\lambda = 10.6\,\mu$m). Since these wavelengths cannot be transmitted well through optical fibers, they are mainly used for ablation at tissue surfaces in air. For ablation inside the human body, XeCl excimer lasers ($\lambda = 308$ nm), thulium:YAG lasers ($\lambda = 2.0\,\mu$m) and holmium:YAG lasers ($\lambda = 2.1\,\mu$m) are frequently employed because their radiation is transmitted by low-OH quartz fibers.

The thermal and mechanical transients generated during the pulsed laser ablation process can result in *dynamic changes of the optical absorption properties*, as described in detail in Chapter 9. These changes are particularly important for wavelengths around the absorption peak of water at $\lambda = 2.94\,\mu$m that shifts towards shorter wavelengths for increasing temperature [10–12]. Figure 14.2b shows the variation in optical penetration depth with incident radiant exposure for $\lambda = 2.94$ and 2.79 μm [1]. For $H_0 > 0.5$ J/cm^2, Er:YSGG laser radiation ($\lambda = 2.79\,\mu$m) offers better spatial confinement of the laser energy compared to Er:YAG laser radiation ($\lambda = 2.94\,\mu$m), opposite to the behavior one would expect from the absorption coefficients measured at small radiant exposures (Chapters 3 and 9). Variations in optical absorption with temperature are also important for ultraviolet laser ablation. Absorption of UV radiation by peptide bonds is followed by heating of the surrounding water, resulting in a change in hydrogen bonding structure of water and thus to a red shift of the water absorption band, which at room temperature is located at 160 nm [13]. The absorption of water at $\lambda = 193$ nm may be raised to as much as $\mu_a \approx 10^4$ cm^{-1} at a volumetric energy density of $W = 2$ kJ/cm^3 [13].

Phase transitions of the tissue water are strongly influenced by the *mechanical tissue properties*. Figure 14.3 provides stress-strain curves for a variety of soft biological tissues. Although the mechanical characteristics vary considerably, these tissues all possess a nonlinear stress-strain characteristic with a "concave-up" shape. As a result, biological tissues are soft and elastic under physiologic conditions but become very stiff when loaded in an extreme fashion as in laser ablation.

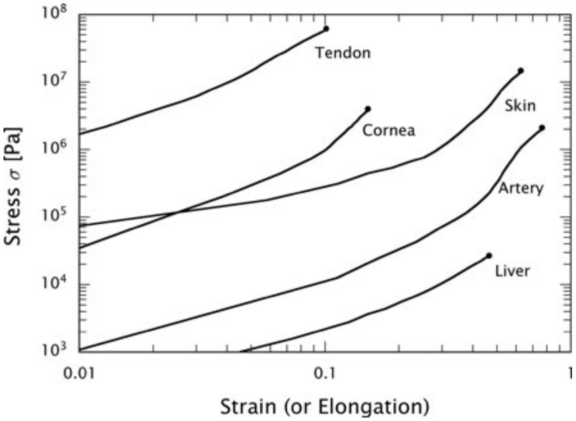

Fig. 14.3 Stress-strain curves characterizing the mechanical properties of various biological tissues under uniaxial tension. The · symbols represent the mechanical state at which tissue fracture occurs. Data are compiled from Ref. [14]

There is a positive correlation between tissue strength and collagen content. Tissues that represent extremes of mechanical strength are the liver and tendon. Liver is a cell-continuous tissue with little ECM and collagen content, which results in a very low ultimate tensile strength (UTS) of 23 kPa and moderate extensibility at fracture ~50% [3, 15]. Tendon is a matrix-continuous tissue that possesses high collagen content. This provides for high strength and stiffness with an UTS of $\gtrsim 100\,\mathrm{MPa}$ and fracture extensibility of ~10%. Skin has similarly high collagen content (25–33%) but lower UTS (~10 MPa) and much larger fracture extensibility of ~30–100% because the collagen fibrils in the dermis are "wavy" and form a loose three-dimensional network [3] (see Fig. 14.1).

Nearly all tissue mechanical data have been acquired under "quasi-static" loading conditions in which the tissue is deformed at very slow strain rates; typically on the order of $10^{-3}\ \mathrm{s}^{-1}$. However, the processes involved in pulsed laser ablation of tissue produce extremely high strain rates; on the order of 10^5–$10^7\ \mathrm{s}^{-1}$. Studies performed to examine the effect of strain rate in the range 0.3–170 s^{-1} have revealed that while the tissue strain at fracture remains roughly constant, the UTS increases in proportion to the logarithm of the strain rate [15–17]. The increase in UTS is due to the viscous dissipation between the collagen fibrils and the adjacent ground substance during the rapid deformation. It is not known whether the logarithmic dependence of tissue UTS vs. strain rate remains valid at the extreme rates produced by pulsed laser ablation. However, the available UTS data suggest that the tissue strength under ablative conditions can be considerably higher than that measured under "quasi-static" loading conditions.

Thermal denaturation of collagen fibrils affects the dynamics of the ablation process. Denaturation begins when the thermal energy of the constituent molecules overcomes the weak hydrogen bonds and van der Waals interactions stabilizing the helical configuration of the α-chains in the collagen molecule [18]. The "native" triple-helical structure of the molecule is thus transformed into a "denatured" random coil structure that is associated with a loss of the banding pattern of the native collagen fibrils in TEM (see Fig. 14.1) and with shrinkage of the fibrils along their longitudinal axis [4, 19]. However, when the fibrils are embedded in the surrounding tissue, shrinkage is impaired and tensile stress develops along the fibrils due to the covalent cross-links that connect the molecules and maintain the organization of the fibrils [20, 21]. Further heating denatures first the thermally-labile and then the thermally-stable covalent cross-links between the collagen molecules. This results in a stepwise disintegration of the collagen fibrils [22], a relaxation of the stresses developed during shrinkage [20, 21], and, finally, in total mechanical failure of the fibrillar tissue structure that now appears homogeneous in TEM [18, 19]. Older tissues possess a higher density of cross-links and thus require higher temperatures to undergo these transitions [4, 23].

To understand the degree to which collagen denaturation influences a particular ablation process, one must consider the kinetics of this rate process (see Chapter 13) that depends on both the magnitude and duration of thermal exposure [24]. For shorter heating times, considerably higher temperatures are required for denaturation. While the mechanical stability of collagen is destroyed at about 75°C when heated for several minutes [20], temperatures far in excess of 100°C are required to affect mechanical stability for thermal exposures in the nanosecond to microsecond range characteristic of pulsed laser ablation [25]. Nevertheless, given that surface temperatures approaching 400–750°C have been measured during tissue ablation using laser pulses of 100 μs duration [26], the mechanical integrity of the tissue ECM will certainly be compromised. We shall see in Section 14.6 that the progressive denaturation of the tissue matrix with time is one reason for the continuation of the ablation process after the end of the laser pulse. In nanosecond ablation even moderate radiant exposures may produce temperatures that exceed 1000°C in the superficial tissue layer, at which point the mechanical integrity of the tissue ECM is completely lost due to thermal dissociation of the constituent molecules into volatile fragments [27] (Section 14.4.6).

14.3 Linear Thermo-Mechanical Response to Pulsed Irradiation

In the absence of photochemical processes, the laser energy absorbed by the tissue is completely converted to a *temperature rise* before a phase transition occurs. Under adiabatic conditions, the temperature rise T [K] at a location r is related to the local volumetric energy density $W(r)$ [J/m^3] by:

$$\Delta T(r) = \frac{W(r)}{\rho c_v} \tag{14.1}$$

where ρ[kg/m^3] is the tissue density and c_v[J·kg^{-1}·K^{-1}] the specific heat capacity at constant volume. The absorbed energy is redistributed by thermal diffusion [28] (see Chapter 10). In 1983, Anderson and Parrish introduced the concept that spatially-confined microsurgical effects can be achieved by using laser pulse durations t_p shorter than the characteristic thermal diffusion time of the heated volume [29]. For laser ablation, the heated volume is typically a layer with a thickness of the optical penetration depth $(1/\mu_a)$, and the characteristic thermal diffusion time t_d is given as [30]

$$t_d = \frac{1}{\kappa \mu_a^2} \tag{14.2}$$

where κ [m^2/s] is the thermal diffusivity. By defining a dimensionless ratio $t_d^* = (t_p/t_d)$, the thermal confinement condition can be expressed as [31, 32]

$$t_d^* = \frac{t_p}{t_d} = \kappa \mu_a^2 t_p \lesssim 1 \tag{14.3}$$

Short-pulse laser irradiation of tissue not only leads to rapid heating but also to the *generation and propagation of thermoelastic stresses* [33]. The magnitude and temporal structure of these stresses are governed by the longitudinal speed of sound in the medium c_a, the laser pulse duration t_p, the depth of the heated volume $(1/\mu_a)$ and the Grüneisen coefficient Γ [33, 34]. The dimensionless Grüneisen coefficient Γ is simply the internal stress per unit energy density generated when depositing energy into a target under constant volume (i.e., isochoric) conditions. This is given by the thermodynamic derivative

$$\Gamma = \left(\frac{\partial \sigma}{\partial W}\right)_v = \frac{\beta}{\rho c_v \kappa_T} \tag{14.4}$$

where σ [Pa] is the internal stress, W the volumetric energy density, v the specific volume, β [1/K] the coefficient of thermal expansion, ρ the mass density, c_v the specific heat capacity at constant volume and κ_T [1/Pa] the isothermal compressibility.

Thermoelastic stresses are most prominent when the laser pulse duration t_p is smaller than the characteristic time required for a stress wave to traverse the heated volume $t_m = (1/\mu_a c_a)$ [30]. This means that the stresses are confined within the heated region during the laser irradiation. By defining a dimensionless ratio $t_m^* = (t_p/t_m)$, the “stress confinement” condition can be expressed as [31, 32]

$$t_m^* = \frac{t_p}{t_m} = \mu_a c_a t_p \lesssim 1 \tag{14.5}$$

For $t_m^* << 1$, heating of the laser-affected volume occurs under isochoric conditions and the thermoelastic stress is maximal. The peak stress σ_p is given by [33]

$$\sigma_p = A\Gamma\varepsilon_0 = A\Gamma\mu_a\Phi_0 \tag{14.6}$$

where $A = 1$ and the duration of the thermoelastic stress transient t_a scales with the stress propagation time and $t_a \approx (4 - 6/\mu_a c_a)$. When the stress transient leaves the heated volume, the peak stress drops to 0.5 σ_p.

In the limit $t_m^* \rightarrow \infty$, where there is no stress confinement, $A \rightarrow 0$ and the duration of the stress transient approaches that of the laser pulse. The variation of A with t_m^* for different temporal laser pulse shapes is shown in Fig. 14.4.

While thermal expansion of a heated volume generates compressive thermoelastic stresses, subsequent propagation of these stresses results in transients that contain both compressive and tensile components. Tensile stresses arise from the reflection of the compressive stress waves at an interface with a medium with lower acoustic impedance (tissue-air, tissue-water) or from the three-dimensional characteristics of acoustic wave propagation from a heated tissue volume of finite size [2, 34, 36–39]. Tensile stress wave generation originating from acoustic impedance mismatch at a tissue surface is shown in Fig. 14.5.

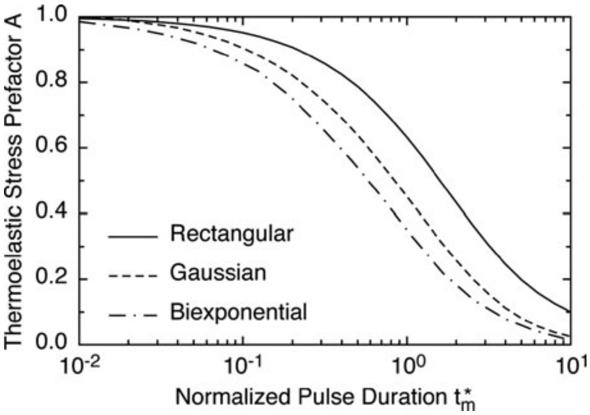

Fig. 14.4 Variation of the thermoelastic stress prefactor A (see Eq. (14.8)) with pulse duration relative to the stress propagation time across the heated volume t_m^* for various laser pulse shapes. Data are compiled from [33] and [35]

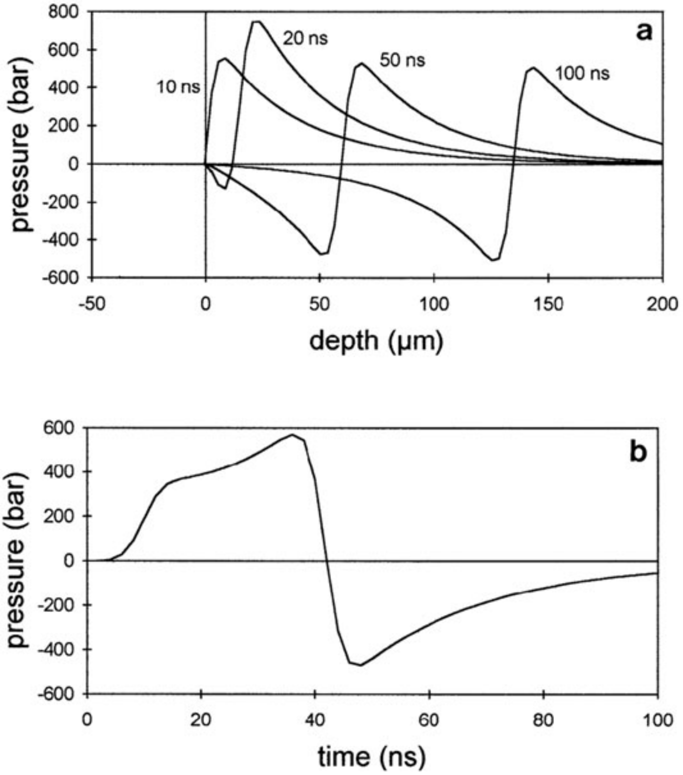

Fig. 14.5 (**a**) Development of a thermoelastic stress wave in water calculated for $H_0 = 2$ J/cm^2; $\mu_a = 200$ cm^{-1} and $t_p = 8$ ns. (**b**) Pressure as a function of time at a depth of 50 µm. (Reprinted with permission from [37])

14.4 Thermodynamics and Kinetics of Phase Transitions

All ablation processes involve the fracture of chemical bonds and lead to the removal of single molecules, molecular fragments, and molecular clusters. Bond fracture can also produce the formation of voids (i.e., bubbles or cracks) that facilitate the ejection of non-decomposed material fragments upon mechanical failure of the target. Vaporization, molecular fragmentation, and void formation can all be viewed as phase transitions that are accomplished via photothermal, photomechanical, and/or photochemical mechanisms. Given the central role of phase transitions in the ablation process, we devote this section to a systematic presentation and analysis of their thermodynamics and kinetics. We begin by considering the generation of phase transitions via photothermal and photomechanical phenomena and their modification in the presence of a tissue matrix. We then end the section with a treatment of photochemical mechanisms to achieve bond dissociation.

14.4.1 Phase Diagrams

We use the pressure vs. temperature projection of the phase diagram for liquid and gaseous water (Fig. 14.6) and the pressure vs. specific volume projection of the thermodynamic phase diagram (Fig. 14.7) to discuss the thermodynamics of phase transitions. The solid curve *A–C* on Fig. 14.6 represents those pressure/temperature pairs where liquid and vapor phases are in equilibrium with each other and is known as the “binodal.” The curve *B–C–D*, the “spinodal,” denotes a locus of states representing the intrinsic stability limit of the liquid or vapor phase [i.e., $(\partial T/\partial s)_p = 0$ and $(\partial p/\partial v)_T = 0$]. At the spinodal, the superheated liquid phase (*B–C*) or subcooled vapor (*C–D*) phase is no longer stable with respect to the random density

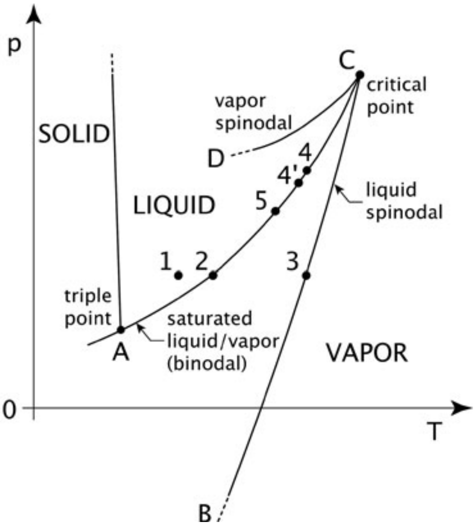

Fig. 14.6 Pressure vs. temperature projection of the thermodynamic phase diagram including the spinodal curve. Specific states of interest are (1) ambient temperature and pressure, (2) boiling temperature under ambient conditions, (3) spinodal temperature at ambient pressure, (4) saturated conditions corresponding to the ambient spinodal temperature. The importance of points 4′ and 5 are discussed in Section 14.4.4

Fig. 14.7 Pressure vs. specific volume projection of the thermodynamic phase diagram including the spinodal curve and equilibrium and van der Waals isotherms. Points 1–4 correspond to those shown in Fig. 14.6. Importance of points 4′, 5, 5′ and the isoenthalp are discussed in Section 14.4.4

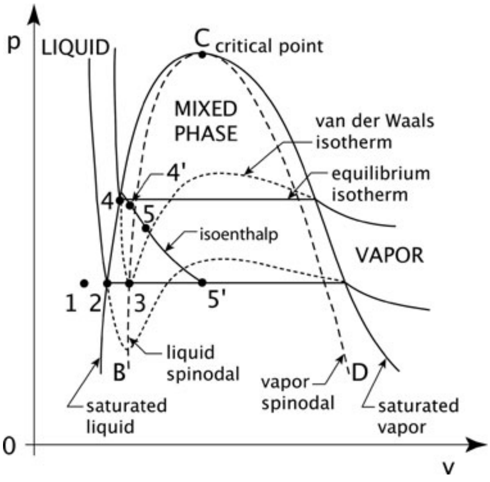

fluctuations that are present in all materials at nonzero temperatures. The region between segment *A*–*C* of the binodal and *B*–*C* of the spinodal represents metastable states of the superheated liquid for which the presence of a free surface or bubble nucleus is required for vaporization. The binodal and spinodal curves intersect at the critical point *C*, above which no thermodynamic distinction can be made between liquid and vapor phases. For water, the critical point is located at $T_c = 374.14°\mathrm{C}$ and $p_c = 22.09$ MPa.

Liquid, vapor, and mixed phase regions are clearly demarcated in the *p*-*v* diagram of Fig. 14.7. The binodal encompasses the mixed phase region that specifies the range of specific volumes in which liquid and gaseous phases coexist for a given pressure and temperature. The dashed curve provides the spinodal where the segment *B*–*C* represents the stability limit of superheated liquid and segment *C*–*D* represents the stability limit of subcooled vapor.

14.4.2 Surface Vaporization

Equilibrium vaporization at a liquid-vapor interface is associated with an increase of specific volume at constant temperature that requires the latent heat of vaporization. This process can occur at any single location along the binodal (A–C) in the *p*-*T* diagram of Fig. 14.6, with the rate of vaporization increasing with *T*. In the *p*-*v* diagram in Fig. 14.7, surface vaporization is represented by a path following an equilibrium isotherm that connects a state of saturated liquid with a state of saturated vapor. Thus vaporization does not occur at a pre-determined temperature and theoretical models that adopt a fixed “vaporization temperature” violate the basic physics of the process [40]. The actual surface temperature is dictated by the rate of equilibrium vaporization that balances the irradiance supplied to the system. Thus, surface vaporization becomes a “cooling” heat flux boundary condition in models describing the thermal distribution within the sample.

However, during laser ablation, rates of vapor formation in excess of that predicted by equilibrium vaporization are often achieved. This occurs because the increased equilibrium vapor pressure corresponding to the increased temperature of the liquid surface is not established instantaneously. This results in an increased mass flux of vapor transported into the surroundings is known as non-equilibrium interphase mass transfer and can be estimated using arguments from the kinetic theory of gases [41, 42]. Nevertheless, even this increased non-equilibrium interphase mass transfer provides a very small ablation rate. *Efficient* ablation is achieved at laser irradiances that deposit energy at rates that cannot be balanced by surface vaporization processes alone. This results in material removal via *volumetric* processes.

14.4.3 Normal Boiling

Normal boiling refers to a volumetric process that forms vapor at a thermodynamic state on the binodal as indicated by point 2 in Fig. 14.6. Thus, for a given pressure, the binodal defines the corresponding “boiling temperature.” For water at atmospheric pressure this temperature is 100°C. However, for ablation processes with a high rate of mass removal, the boiling temperature is increased significantly because the recoil increases the pressure both at the target surface and within its bulk.

Vapor formation in normal boiling relies on the presence of pre-existing nuclei of vapor or dissolved gas within the liquid to catalyze the nucleation and growth of vapor bubbles. The transition from saturated liquid to saturated vapor occurs within a finite layer of mixed phase. The thickness of this “vapor-liquid” layer is comparable to the optical penetration depth of the incident radiation, and its composition varies from that of saturated liquid at its base to saturated vapor at the target surface [40, 43]. As a result, the surface temperature is fixed at the saturation conditions corresponding to the pressure at the target surface and there is no temperature gradient within the vapor-liquid layer.

Once a normal boiling process is established, temperatures slightly higher that the saturation temperature result in a growth of the vapor bubbles in the liquid. Therefore, normal boiling processes *always “involve” partial vaporization* of a liquid volume through the growth of vapor bubbles. Thus the concept sometimes found in biomedical ablation papers that vaporization only occurs once the entire latent heat of vaporization is deposited is not correct.

Nevertheless, normal boiling plays a negligible role for pulsed laser ablation for two reasons. First, the density of heterogeneous bubble nucleation sites is likely insufficient to provide a boiling process sufficiently vigorous to balance the high rates of energy deposition achieved in most pulsed laser ablation processes [32, 40]. Second, the high rates of energy deposition can be balanced only if the bubbles move to the target surface on a time scale set by the propagation velocity of the ablation front. Miotello and Kelly [44] showed that this is not possible when irradiating pure water with nanosecond laser pulses and is possible for microsecond pulses only for radiant exposures proximal to the ablation threshold. In tissue this is even less likely because the mobility of vapor bubbles is further inhibited by the presence of the extracellular matrix.

14.4.4 Phase Explosion and Explosive Boiling

When the rate of volumetric energy deposition provided by laser radiation is more rapid than the rate of energy consumed by vaporization and normal boiling, the tissue water is driven to a metastable superheated state. The superheated liquid is metastable until the spinodal temperature is reached. The spinodal limit is defined by line *B*–*C* in Fig. 14.6 that represent the locus of states with infinite compressibility $[(\partial p/\partial v)_T = 0]$. At the spinodal limit, the superheated liquid undergoes "spinodal decomposition:" a spontaneous process by which a thermodynamically unstable liquid relaxes towards equilibrium by "phase separation" into a mixture of saturated vapor and saturated liquid [45–47]. The spinodal temperature of water at atmospheric pressure is ≈305°C with the corresponding equilibrium saturation vapor pressure of 9.2 MPa. Thus spinodal decomposition under atmospheric conditions involves an impressive pressure rise resulting in the violent emission of saturated liquid droplets by the expanding vapor.

For the phase diagram shown in Fig. 14.6, the heating phase corresponds to the path $1 \rightarrow 3$, and the spinodal decomposition will initially result in a nearly isochoric transition from point 3 on the spinodal to point $4'$ in the mixed phase region possessing the same enthalpy. For pure water, the subsequent explosive expansion of this mixture will transition through a series of thermodynamic states that follows the curve of constant enthalpy (isoenthalp), as shown in Fig 14.7, until the mixture reaches atmospheric pessue at point $5'$. During the expansion $4' \rightarrow 5'$, the temperature of the mixture drops to 100°C, and about half of the liquid is transformed into vapor. The vapor fraction (∼49.6%) is given by energy density necessary to heat water from room temperature to the spinodal limit (1.27 kJ/g) as compared to the sum of the sensible and latent enthalpy of vaporization. The remaining saturated liquid is ejected in the form of droplets.

To provide a complete description of the phase transformation process as the liquid is heated to the spinodal limit, one must also consider the potential contribution of homogenous nucleation [32, 44, 48–50]. Homogenous nucleation refers to the spontaneous formation of vapor inclusions within the bulk liquid that arise solely from thermodynamic fluctuations and is not catalyzed by the presence of impurities or dissolved gas. While the formation of such vapor "nuclei" is spontaneous, their growth is not ensured and depends strongly on superheat temperature.

In classical nucleation theory, the driving force for growth of vapor nuclei is supplied by the difference in chemical potential between the superheated liquid outside the bubble and the vapor inside the bubble. This driving force is necessary to overcome the free energy barrier posed by the surface tension separating the vapor from the liquid [47]. The chemical potential difference between the superheated

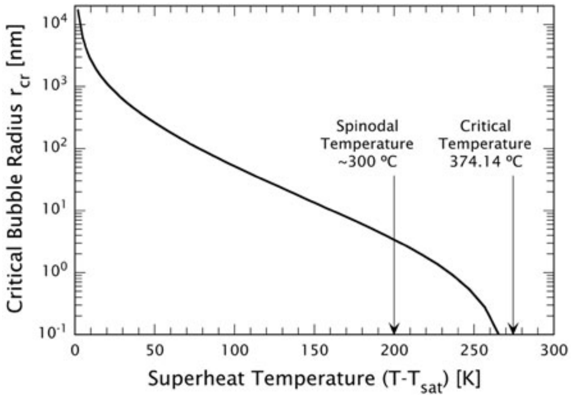

Fig. 14.8 Variation of the critical bubble radius r_{cr} required for spontaneous vapor bubble growth with superheat temperature. Note that the critical bubble radius goes to zero at the critical temperature

liquid and vapor scales with the bubble volume (i.e., r^3), while the contribution from surface tension scales with the bubble surface area (i.e., r^2). As a result, small vapor nuclei that form due to thermodynamic fluctuations spontaneously collapse while larger vapor nuclei will grow. The Gibbs free energy ΔG that describes the thermodynamics of bubble formation is given by:

$$\Delta G = \frac{4\pi r^3}{3}(\mu_v - \mu_l) + 4\pi r^2 \sigma \tag{14.7}$$

where μ_v and μ_l [J/m^3] are the chemical potentials of the vapor and liquid state, respectively, r is the radius of the vapor nuclei, and σ [N/m] is the surface tension of the surrounding liquid [47, 51]. Nuclei grow if they are larger than a critical radius r_{cr}. Figure 14.8 shows the dependence of r_{cr} on superheat temperature for water. Note that while r_{cr} strongly decreases as the superheat temperature increases, it remains finite even at the spinodal temperature. Thus nucleation remains an activated process with a finite free energy barrier [45]. The strong reduction of Δr_{cr} results in a dramatic rise in the nucleation rate J [s^{-1}] with the superheat temperature that attains a large, but finite, value at the spinodal temperature as shown in Fig. 14.9. Here we define nucleation as formation of a bubble with radius $r > r_{cr}$. The energy barrier that must be overcome for the conversion from the liquid to vapor phase disappears only when surface tension disappears and this occurs at the critical point. To account for the influence of statistical fluctuations on the stability limit, Kiselev has introduced the concept of a *kinetic spinodal*. The kinetic spinodal is defined as the locus of thermodynamic states where the time for spontaneous formation (driven by superheat temperature) of vapor nuclei becomes smaller than the characteristic time for their decay to local equilibrium (driven by surface tension) [52]. The superheat temperatures defined by the kinetic spinodal are much lower than the critical temperature and slightly lower than the classical spinodal. The kinetic spinodal represents the physical limit of metastable liquid states that can be achieved prior to spinodal decomposition.

Fig. 14.9 Variation of vapor bubble nucleation rate with superheat temperature. Nucleation is here defined as formation of a bubble with radius $r > r_{cr}$ (see Fig. 14.8)

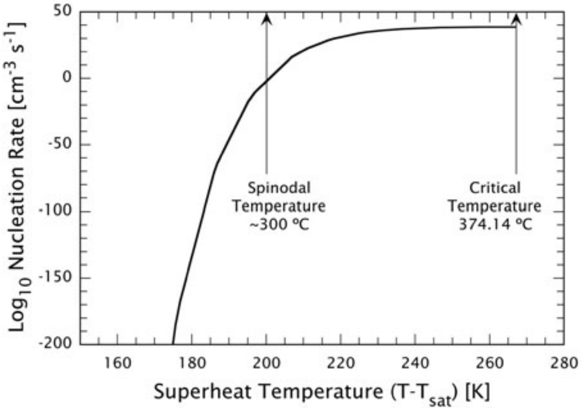

Thus, in general, the transformation of superheated (metastable) liquid to an equilibrium state of mixed phase may involve both bubble nucleation (large density fluctuations extending over a small spatial extent) and spinodal decomposition (small density fluctuations extending over a large spatial extent). We refer to the collective phase transition process as a *phase explosion*. A more detailed consideration of nucleation theory and spinodal decomposition as it relates phase transitions and tissue ablation can be found in our earlier review [1].

Thus far we have focused on processes tracing a path indicated by $1 \rightarrow 3 \rightarrow 4' \rightarrow 5 \rightarrow 5'$ in Figs. 14.6 and 14.7. This path corresponds to the extreme case in which no vapor nuclei are present in the liquid. When the heating occurs very rapidly at high radiant exposures, the liquid experiences a recoil pressure from surface vaporization/interphase mass transfer that can be substantial due to the nonequilibrium conditions produced during the beginning of the laser pulse. Thus spinodal conditions are reached at an elevated pressure somewhere between point 3 and the critical point C. Because the resulting phase explosion occurs at elevated temperature and pressure, the pressure jump associated with the phase separation is less severe. The elevated temperature corresponds to a higher volumetric energy density of the superheated liquid, and therefore more than half of the liquid will be transformed into vapor during the phase separation process.

When vapor nuclei are present in the liquid and the heating occurs on a time scale such that a significant fraction of the incident laser energy (but not the entire energy) contributes to the growth of heterogeneous and homogeneous vapor nuclei, the resulting phase transition process again follows a path that is intermediate between normal boiling and the path $1 \rightarrow 3 \rightarrow 4$. Spinodal conditions in the superheated liquid are again reached at a location between point 3 and the critical point C followed by phase separation. In this case however, the pressure rise is due to vapor formation at the nucleating centers rather than recoil from vapor leaving the target surface. Such intermediate processes are termed *explosive boiling*. In general, the energy necessary to reach spinodal conditions is higher for explosive boiling than for a phase explosion with surface vaporization. The amount of vapor formation is greater due to contributions from both the growing nucleation centers and the phase separation.

Both phase explosion and explosive boiling are volumetric processes in which a portion of the target material is ejected in the liquid phase and the latent heat of vaporization is not supplied to the entire ablated mass. As a result, the ablation efficiency (mass removed by a given amount of laser energy) is higher for these processes as compared to surface vaporization and normal boiling where all material is removed in the vapor phase.

14.4.5 *Effects of the Tissue Matrix on the Phase Transitions*

In pulsed laser ablation of tissues, the phase transition processes are affected by the presence of the extracellular tissue matrix (ECM). For boiling processes within tissue, the vapor pressure necessary to drive bubble growth must not only overcome surface tension but also the elasticity of the tissue matrix [53]. Therefore, bubble growth in tissue requires a higher internal pressure than in pure liquids, and the elevated pressure is coupled to an increase in the boiling (saturation) temperature. The pressure increase that develops during the boiling process continues until it exceeds the ultimate tensile strength of the ECM and results in explosive tissue ablation [53]. We term this process *confined boiling*. On the *p*-*T* phase diagram in Fig. 14.10, the confined boiling process corresponds to a path 1→2→6, where the 2→6 transition is coincident with the binodal and terminates where the saturated vapor pressure equals the ultimate tensile strength of the tissue. In the presence of a tissue matrix, explosive material ejection will thus occur regardless of the rate of energy deposition. Thus, it is not surprising that explosive material ejection due to confined boiling has also been reported to occur in ablation using continuous irradiation at relatively low irradiances [54, 55].

In the above scenario, little vaporization occurs prior to the onset of ablation because bubble growth is impeded by the necessity to deform the tissue matrix. For

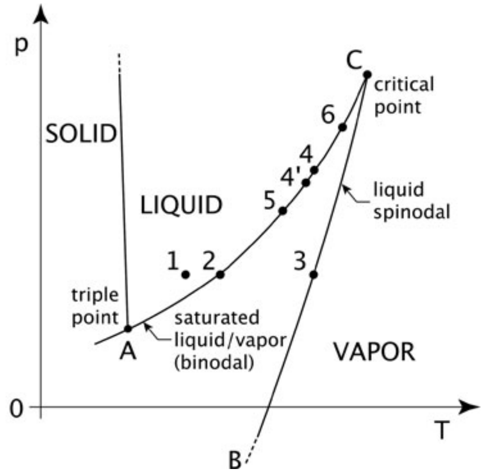

Fig. 14.10 Path taken through the *p* vs. *T* projection of the thermodynamic phase diagram for confined boiling (1 → 2 → 4 → 6) and for tissue ablation involving a phase explosion (1 → 2 → 3 → 4′ → 5 → 6). The actual path followed depends on the rate of energy deposition, number density of heterogeneous nuclei, and the mechanical strength of the tissue matrix relative to the saturation vapor pressure corresponding to the ambient spinodal temperature

mechanically weak tissues, much of the ejected mass consists of tissue that is fragmented and accelerated by the phase explosion. As a result, the ablation enthalpy can thus be considerably smaller than the vaporization enthalpy of water. However, for tissues that possess a strong matrix (e.g., skin), temperatures of 400–700°C are required to produce a saturation vapor pressure exceeding the ultimate tensile strength to initiate ablation [26]. Under these conditions, the ablation enthalpy often exceeds the vaporization enthalpy of water.

The tissue matrix retains its mechanical integrity during nanosecond or microsecond laser exposures even for temperature rises of several hundred degrees. There are several factors that are responsible for this. First, as discussed in Section 14.2, the temperatures required for disintegration of the matrix increase strongly as the duration of heat exposure decreases. Second, the application of tensile stresses to collagen fibrils stabilizes the helical architecture and results in a significant increase of the denaturation temperature. Thus the generation of tensile stresses resulting from pulsed laser heating is expected to further stabilize a collagen matrix with respect to possible collagen denaturation. Third, the extreme strain rates produced by pulsed laser ablation processes ($\sim 10^5 - 10^7\ \mathrm{s}^{-1}$) likely increase the ultimate tensile strength of the tissue matrix (see Section 14.2). Thus ablation does not involve a "liquefaction" of the tissue as assumed in earlier models [56, 57] but proceeds via the ejection of tissue fragments driven by the vaporization of tissue water.

For low rates of volumetric energy deposition $S = \mu_a \phi$ [W/cm^2] and high number densities of heterogeneous nuclei, the nature of the ablation process is largely independent of tissue mechanical properties. The laser irradiation will initially heat the tissue under equilibrium conditions at constant pressure ($1 \rightarrow 2$) and then continue on the binodal until the ultimate tensile strength of the tissue is reached; resulting in explosive material removal. However, if the tissue is heated rapidly and/or a small number density of heterogeneous nuclei are present, the tissue water will be driven into a metastable state and a phase explosion will be initiated when the spinodal limit is reached ($1 \rightarrow 2 \rightarrow 3 \rightarrow 4' \rightarrow 5$). The subsequent evolution of the process now depends on the mechanical properties of the tissue. Immediate material ejection will result for tissues that are unable to withstand the stresses and deformations associated with the phase explosion. However, tissues possessing high collagen content, and thus high UTS, will not fail mechanically due to the phase explosion. The laser irradiation will then drive a confined boiling process as indicated by path ($5 \rightarrow 6$) in Fig. 14.10 until the tissue ruptures at higher vapor pressures resulting in material removal. For pulsed ablation of skin, surface temperatures of 400–750°C have been measured [26] indicating that the dynamic tensile strength of the tissue matrix is higher than the pressure at the critical point ($p_c = 22.09$ MPa).

14.4.6 Vapor Explosion and Photothermal Dissociation of the Tissue Matrix

For ablation using nanosecond pulses, the volumetric energy densities achieved in the tissue water usually exceeds the vaporization enthalpy of water [27, 32]. Under these conditions, the liquid water is completely transformed into vapor in a process termed *vapor explosion*. Moreover, at temperatures exceeding ∼1000°C the constituent molecules of the extracellular matrix are thermally dissociated into volatile fragments. Energetically, these processes result in an ablation enthalpy higher than the vaporization of water and are "less efficient" than phase explosion or confined boiling because they do not involve the ejection of condensed material.

An important factor contributing to the high volumetric energy densities achieved in nanosecond laser ablation is the recoil pressure produced by the ablation of superficial layers of the target. At the beginning of laser exposure, ablation is governed by non-equilibrium surface vaporization. During this phase the recoil pressure is relatively small and a phase explosion occurs as soon as the temperature reaches the spinodal limit. With the onset of the phase explosion, the ablation has transformed from a surface-mediated to a volumetric process resulting in a rapid increase of the recoil stress. This large compressive stress inhibits the ablation of deeper tissue layers until the volumetric energy density is sufficiently high to cause a phase transition that can overcome these higher pressures. Therefore the phase transition of subsurface tissue layers will be more vigorous than the initial surface vaporization because a larger volumetric energy density is required to initiate the phase change process. This, in turn, produces a higher recoil pressure that impedes ablation in deeper tissue layers until even higher volumetric energy densities are reached. At any given depth, ablation starts as soon as the vapor pressure exceeds the recoil pressure resulting from the explosive removal of more superficial layers. This results in a "positive-feedback" process in which the volumetric energy density and pressure values required for the onset of ablation at deeper tissue layers will continue to increase as long as the laser irradiance is increasing within the laser pulse. After the peak irradiance of the laser pulse has passed, the volumetric energy density and pressure at the target surface will decrease while the ablation front continues to propagate into the target. The ablation process becomes most vigorous shortly after the peak of the laser pulse, as that is when the volumetric energy density in the target reaches a maximum value [27]. Since the evolution of thermodynamic states within the target is determined both by the incident laser irradiation and by the recoil produced by the ablation plume, ablation will likely continue well beyond the end of the laser pulse [1, 27, 58]. When the volumetric energy density in the target drops below the value required for thermal dissociation of the tissue matrix, the ejection of particulate tissue fragments will commence [27, 58]. Ablation ceases when the vapor pressure within the tissue falls below the ultimate tensile strength of the tissue matrix which itself is influenced by the local denaturation kinetics.

14.4.7 Effect of Stress Confinement on the Ablation Process

When performing ablation under conditions of stress confinement, the thermoelastic stresses modify significantly the phase transition processes that drive material removal. As discussed in Section 14.3, the thermoelastic stress wave propagation results in both compressive and tensile components (Fig. 14.5). The tensile stress component can produce material ejection at temperatures less than 100°C in liquids with heterogeneous vapor/cavitation nuclei and in mechanically weak tissues such as liver. This phenomenon has been compared to back surface spallation produced by high-pressure impact [59, 60] and investigated in several studies [61, 62]. Nevertheless, temperatures above 100°C are usually necessary to initiate efficient tissue removal [61]. The important influence of tensile stress waves at temperatures above 100°C has only recently attracted attention [1, 33]. Figure 14.11 shows the path taken through the *p–T* phase diagram for a temperature rise above 100°C produced by laser irradiation with stress confinement. A heating phase (1→2), coupled with the generation of compressive stress, is followed by the passage of a tensile stress wave (2→3) that leads to a crossing of the spinodal limit, resulting in a phase explosion. The passage of the stress wave is followed by explosive boiling into the large number of bubbles produced shortly before (point 4), resulting in vigorous material ejection. This ejection occurs at temperatures lower than the spinodal temperature at atmospheric pressure (T=305°C) because, as shown in Fig. 14.11, the spinodal temperature is reduced with the decrease in pressure provided by the tensile thermoelastic stresses. It is important to note that the sequence of events described above may occur not only during surface ablation in a gaseous environment but also when laser pulses are focused into a transparent material. In fact, this process provides the basis of the high precision in femtosecond laser nanosurgery of cell [2].

At volumetric energy densities in excess of the spinodal limit at ambient pressure, i.e., for T>300°C, the superheated liquid is unstable and the onset of explosive ablation need not be initiated by the tensile component of the thermoelastic stress. Nevertheless, the thermoelastic stress transient can still contribute to material removal. The magnitude of thermoelastic transients produced by a given

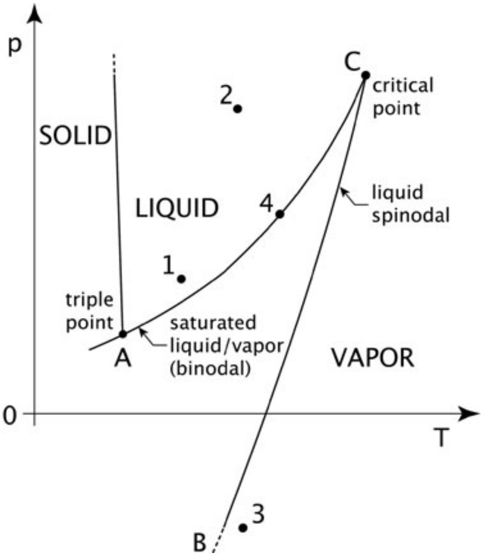

Fig. 14.11 Path taken through the *p* vs. *T* projection of the thermodynamic phase diagram for a temperature rise above 100°C under stress confinement conditions. The transition 1→2 corresponds to the heating phase that is coupled with the generation of compressive stress. The transition 2→3 corresponds to the passage of the tensile stress wave that leads to a crossing of the spinodal limit resulting in phase separation. After the passage of the stress wave, the system reaches point 4 that corresponds to explosive boiling into the large number of bubbles produced shortly before

temperature rise under conditions of stress-confinement is much larger than the saturation vapor pressure resulting from the same temperature rise and for $T > 1000°\mathrm{C}$ may well exceed 1 GPa. The compressive component of the thermoelastic stress wave upon propagation will develop into a shock wave. The propagation of this shock wave into the depth of the target along with energy dissipation at the shock front [63, 64] result in tissue heating at locations beyond those heated directly by the laser irradiation and subsequent heat diffusion. Shock wave propagation thus serves as a form of convective heat transfer that extends the ablation depth and increases ablation efficiency [65]. Experimental evidence for shock wave induced phase changes of water after laser-induced breakdown was provided by Vogel and Noack [66]. For pulsed laser surface ablation, temperatures in the shock wave region will mostly be below the spinodal limit since a pressure jump in the neighborhood of 5 GPa is required to heat water from room temperature to 300°C [63]. Convective heat transfer will become important for ablation only for sufficient large volumetric energy densities and for very high degrees of stress confinement, i.e. very short pulse durations. We conclude that regardless of the volumetric energy density, stress confinement invariably serves to lower the ablation threshold and increase ablation efficiency [1, 33, 61, 65, 67].

14.5 Photochemical Decomposition

In 1982 it was discovered that intense ultraviolet laser pulses can etch synthetic polymer surfaces with sub-micrometer precision and without evidence of thermal or mechanical damage [68, 69]. Within one year, argon fluoride (ArF) excimer laser radiation ($\lambda = 193$ nm) was being explored to cut or reshape the surface of the cornea for the correction of visual defects [70]. To explain the unprecedented ablation characteristics, investigators invoked mechanisms unique to ultraviolet laser radiation. Because the dissociation energies of many organic molecular bonds are smaller than the photon energies (4–6.5 eV) at UV laser wavelengths ranging from $\lambda = 193$–355 nm, Srinivasan and Leigh hypothesized that the UV photons cause direct "bond-breaking" of the absorbing molecular chains in the organic target leading to ablative "photochemical decomposition" [71, 72]. Their theory assumes that material is ablated above a certain threshold irradiance which provides a bond dissociation rate that exceeds the rate of bond recombination [73, 74]. The molecular fragments have a lower density than the native macromolecules, and that creates an internal pressure rise and the ejection of decomposed material [75, 76].

Initially, it was believed that only a photochemical mechanism would provide the observed etching precision [75]. However, photothermal ablation can yield similarly small ablation depths provided that the optical penetration depth is sufficiently small and the conditions for thermal confinement are met [72, 76–78]. It was also believed that photochemical decomposition using UV wavelengths involved characteristics that would easily distinguish it from thermal ablation processes. However, this distinction proved difficult because following electronic excitation via UV absorption, other processes always compete with photochemical dissociation [79, 80]. Principal

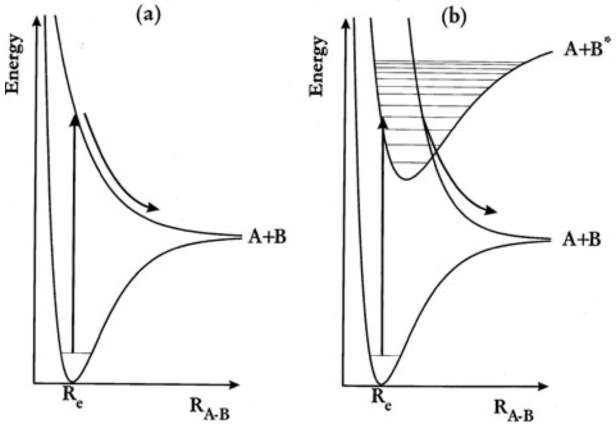

Fig. 14.12 Energy level diagram illustrating various pathways for photochemical bond-breaking. See text for further details. (Reprinted with permission from [80])

amongst these competing pathways is internal conversion of the absorbed photon energy to the vibrational modes of the molecule that is the basis for ablation via photothermal mechanisms.

Two generic types of *photochemical dissociation pathways* of a diatomic molecule A-B are illustrated in Fig. 14.12 [80]. The first type, shown in Fig. 14.12a, is one where electronic excitation promotes the molecule directly into an electronic state with no net bonding and results in a direct dissociation of the molecule into its constituent atoms. The second possibility, shown in Fig. 14.12b, represents a case where the electronic excitation promotes the molecule into a bound excited state matching that of a second, dissociative electronic state. Thus while absorption of the UV photon promotes the molecule into a bound vibrational level within the excited electronic state $A + B^*$, the electronic configuration can acquire the repulsive character of a dissociative state as the bond extends. The bond and repulsive energy potentials shown in Fig. 14.12 imply that for both of these pathways, photon energies significantly larger than the bond energy are necessary to achieve photochemical dissociation. The electronic energy exceeding the binding energy contributes to the kinetic or internal energy of the dissociation products. Therefore, upon thermalization of this excess energy, the ablation products will always be hot even if bond breaking is achieved solely through photochemistry.

Experimental investigations revealed that: (a) regardless of ablation mechanism the ablation fragments are thermalized on time scales comparable to the laser pulse [81]; (b) surface temperatures ranging from 800 to 2200°C are generated during the UV ablation of polymer substrates [82–84]; and (c) the fraction of laser pulse energy that does not manifest as heat in the remaining substrate is completely consumed for the radiation of a blast wave into the surrounding air [85]. While such studies provide strong evidence that a large fraction of the energy provided by UV radiation is thermalized in the substrate and in the ablation plume, they do not exclude the possibility that photochemical processes drive the molecular dissociation process [86].

Further attempts to identify the involvement of photochemical processes in UV ablation were made by examining the reaction products and possible chemical reaction pathways leading to their generation [74, 76, 87, 88]. Investigators expected that if photochemical processes were substantial, the prevalence of smaller molecular fragments would increase with shorter wavelengths because high single photon energy should be capable of breaking bonds of very high energy [76, 86, 89]. Unfortunately, these studies proved inconclusive for many polymers and for tissues as a similar composition of photoproducts is generated by both UV and IR ablation [78, 90]. However, Küper and co-workers' [91] analysis of the reaction pathways and products resulting from UV laser ablation of polymethyl methacrylate (PMMA) provided evidence of a significant photochemical contribution for ArF (λ = 193 nm) and KrF (λ = 248 nm) excimer laser ablation but not for XeCl (λ = 308 nm) excimer laser ablation, and Lippert and Dickinson presented several other examples for a photochemical contribution to polymer ablation [88]. The primary photochemical process in PMMA ablation is the scission of side chains that forms gaseous and volatile fragments. Degradation of the main polymer backbone was found to be a minor contribution relative to the total amount of photoproducts generated and considered to be a photothermal process. Kitai and co-workers [92] introduced the concept that the splitting of the bonds along the backbone of polymer molecules arises from the production of volatile molecules by photochemical scission of side chains. The volatile products possess a larger specific volume than PMMA and fracture the bonds in the main polymer by placing them under stress. The authors argued that the quantum yield of a purely photochemical process is much too low to explain PMMA ablation at the observed threshold radiant exposure [92–94], and that this mechanical decomposition pathway will increase the efficiency of the ablation process. They applied this concept to the physics of UV laser ablation of cornea by assuming that boiling of the water present in the tissue will provide the necessary stresses for the mechanical splitting of the bonds [92].

As a result of these studies and model development [88, 95], it is now generally accepted that UV laser ablation is never driven exclusively by photochemical dissociation and that thermal processes are also present [96]. Photochemical decomposition plays a significant, but not exclusive, role in the ablation of tissues at wavelengths around λ = 200 nm and, for some tissues, is also important at λ = 248 nm. However, its contribution drops rapidly when longer wavelengths are used [77, 97, 98]. Oraevsky and co-workers [98] estimated that the fraction of absorbed XeCl laser energy (λ = 308 nm) contributing to the photolysis of protein is only 2%.

14.6 Ablation Plume Dynamics

The phase transitions described in the previous section drive the formation of a plume consisting of material removed from the ablation site. Usually, the ablation dynamics and plume formation are not governed by just a single type of phase transition but result from an interplay of different transitions occurring at the target surface and in its bulk. The type and strength of the phase transition may change during the laser pulse depending on the volumetric energy densities reached at each target location when the phase change occurs. The characteristics of the ablation plume reflect the underlying ablation dynamics and its analysis provides the insight necessary to draw conclusions about the phase transitions involved in a given ablation event. Furthermore, the plume dynamics influence the ablation process in various ways. The primary ejection of ablation products perpendicular to the tissue surface induces a recoil pressure that may produce additional, secondary material removal processes and cause collateral effects in the bulk tissue. Flow components parallel to the tissue surface that develop at later times may result in a redeposition of ablated material. Scattering and absorption of the incident light by the ablation plume reduce the amount of energy deposited in the target and limit the ablation efficiency at high radiant exposures.

To date, most investigations of the plume dynamics and acoustic phenomena associated with pulsed laser ablation of biological tissues have been performed experimentally by time-resolved photography, probe beam deflectometry, and spectroscopic techniques as reviewed in Refs. [1] and [99]. Here, we focus on the description of the plume dynamics itself rather than on the techniques of investigation. We first discuss the dynamics for water ablation and then progress to the more complicated case of tissue ablation where the primary ablation process and recoil-induced material expulsion are modified by the tissue matrix.

14.6.1 Primary Material Ejection in Nanosecond Ablation

For Q-switched laser pulses of 50–100 ns duration, the rate of energy deposition is extremely large. Close to threshold, the ablation process for liquids such as water is typically characterized by non-equilibrium mass transfer at the target surface [42] followed by a phase explosion of the superficial liquid layer [27]. However, when pulse energies well above the ablation threshold are used, large volumetric energy densities are produced in the target material that result in an ablation process characterized by more vigorous types of phase transitions. To illustrate this, Fig. 14.13 shows the sequence of events in the early phase of Q-switched Er:YAG laser ($\lambda = 2.94\,\mu\text{m}$, $t_p = 70\,\text{ns}$) ablation of water for a radiant exposure of $2.8\,\text{J/cm}^2$; $\approx 25\times$ the ablation threshold. The ablation dynamics is characterized by explosive vaporization followed by shock wave emission and the ejection of very fine droplets. The plume is initially fairly small but rapidly expands shortly after the peak intensity of the laser pulse is reached [47]. As a result, the majority of the ablated material is ejected towards the end and after the laser pulse. The layered structure of the plume reveals that different types of phase transition follow each other as the ablation front propagates into the target. The fact that the top part of the plume is completely transparent indicates that the volumetric energy density in the superficial target layers is larger than the vaporization enthalpy of water at room temperature under atmospheric pressure ($W = 2.59\,\text{kJ/cm}^3$). Therefore, this entire liquid volume is transformed into vapor in a “vapor explosion.” When the ablation front has reached a depth where the energy density becomes smaller than

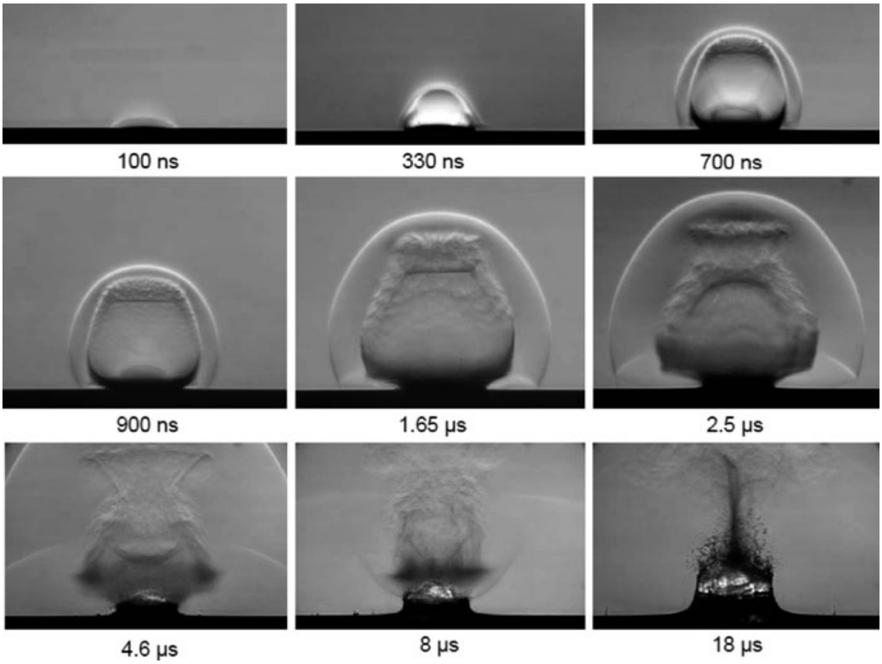

Fig. 14.13 Early phase of water ablation by a Q-switched Er:YAG laser pulse of 70 ns duration, photographed using a novel white light Schlieren technique [99]. The irradiated spot size was 700 μm, the radiant exposure 2.8 J/cm^2 (25x ablation threshold). All times refer to the beginning of the laser pulse. The dynamics is characterized by vapor plume formation, the emission of external and internal shock waves, droplet ejection, and the onset of recoil-induced material expulsion

the vaporization enthalpy of water, the superheated tissue water starts to decompose into vapor and liquid in a phase explosion, and droplet ejection commences. Droplet ejection is first visible after ≈700 ns and lasts for a few microseconds. The droplets cannot be resolved on the photographs and appear as a reddish haze. The reddish color indicates that the droplet size is sufficiently small to cause Rayleigh scattering by which blue light is scattered much stronger than red light [100]. As a consequence, the red spectral components of the illumination dominates the light that passes through the imaging optics. While the droplet ejection still continues, an indentation of the water surface forms and a "splash" region develops at the periphery of the ablation spot due to the recoil pressure produced by the phase transitions (see Section 14.6.3 below).

When soft tissues are ablated at moderate radiant exposures, the entire ablation plume consists of tissue fragments, as illustrated in Fig. 14.14b for Er:YAG laser ablation of liver at $t_p = 70$ ns and a radiant exposure of 1.4 J/cm^2. At the same radiant exposure, the top layer of a water target is already completely vaporized and thus transparent as shown in Fig. 14.14a. At a larger radiant exposure of 5.4 J/cm^2 (Fig. 14.14c), the top part of the plume becomes transparent for both water and liver ablation, and particulate fragments are ejected only after about 200 ns. The sequence

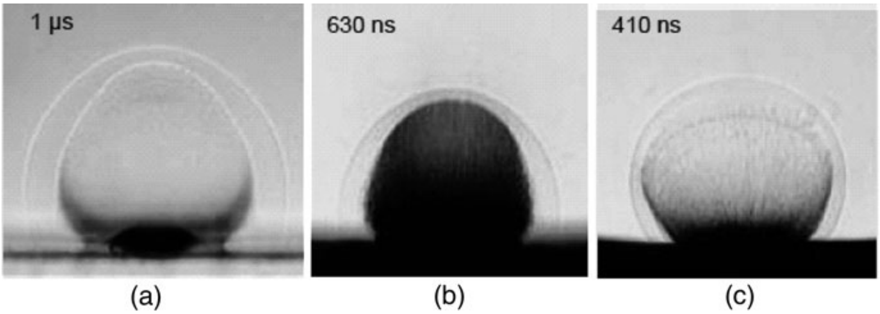

Fig. 14.14 Q-switched Er:YAG laser ablation of (**a**) water at $H = 1.4$ J/cm^2, (**b**) liver at $H = 1.4$ J/cm^2, and (**c**) liver at $H = 5.4$ J/cm^2. The plume consist of water vapor (*top*) and a droplet/vapor mixture in (**a**), tissue fragments in (**b**), and dissociated biomolecules (*top*) and tissue fragments (*bottom*) in (**c**). The volumetric energy densities averaged over the optical penetration depth are ≈ 5.2 kJ/cm^3 in (**a**), ≈ 4 kJ/cm^3 in (**b**), and ≈ 9 kJ/cm^3 in (**c**)

of gaseous ablation products followed by particulates could be visualized only by means of a photographic setup suited for detecting phase objects. In a previous study only the particulate fragments were observed and it was concluded mistakenly that the ablation process commences ≈150 ns after the end of the laser pulse [101]. In reality, the transparency of the top part of the plume indicates that during the initial ablation phase tissue water is completely vaporized and biomolecules are thermally dissociated into volatile fragments, which occurs at temperatures above 1000°C. For the liver target, the subsequent ejection of larger, non-transparent tissue fragments is driven by a phase explosion of the tissue water. The pressure developed during the phase separation (see Section 14.4.5) suffices to rupture the weak tissue matrix in liver parenchyma. The ejection ceases when the ablation front reaches a depth where the temperature drops below the stability limit of the superheated tissue water. The different optical appearance of the transparent and opaque parts of the ablation plume is due to differences in molecular composition and particle size distribution but not necessarily indicative for disparities in the average mass density.

For the ablation of skin at large radiant exposures, a similar sequence of biomolecule dissociation followed by ejection of tissue fragments was observed [27]. However, in this case the ejection of tissue fragments occurred over a shorter time interval than for liver. Ablation ceased when the ablation front reached a depth where the vapor pressure dropped below the tensile strength of the extracellular tissue matrix. Nevertheless, fragment ejection was found to continue for several microseconds after the laser pulse while the tissue matrix is increasingly weakened by thermal denaturation. Generally, the size of the ejected tissue particles is small at early times after the laser pulse and increases with time [27, 101]. The entire sequence of phase transitions occurring during water and tissue ablation is summarized in Fig. 14.15.

Since ablation becomes a volumetric process once the spinodal limit is exceeded and a phase explosion sets in, it is not obvious why large volumetric energy densities

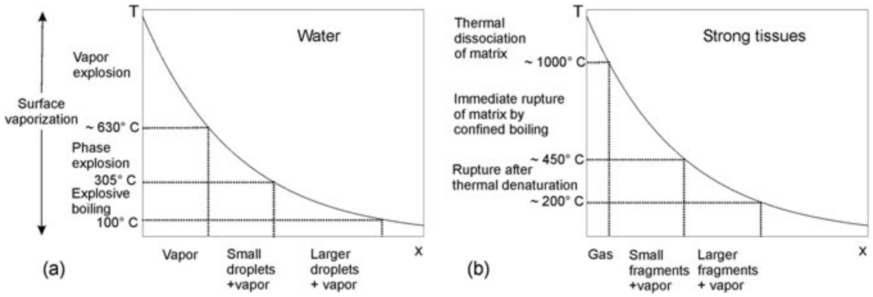

Fig. 14.15 Sequence of phase transitions and corresponding plume constitutents in ablation at radiant exposures well above threshold for (**a**) water ablation, and (**b**) ablation of mechanically strong tissues such as, for example, skin

sufficient for a vapor explosion and dissociation of biomolcules should be reached in pulsed laser tissue ablation. This occurs because the recoil stress produced by the phase transitions of the uppermost tissue layers delays the phase transitions in underlying layers through an increase of the spinodal temperature (see Fig. 14.6). The ongoing absorption of laser energy into the underlying layers can thus drive the thermodynamic state into the supercritical regime. Even larger recoil stresses are produced when these layers are ablated, and the phase transitions in deeper layers are delayed even more. This "positive-feedback" process continues at least until the intensity peak of the laser pulse is reached after which a relaxation process resulting in explosive ablation commences and continues for several microseconds after the end of the laser pulse. The energy densities generated during the runaway process are in the order of 10 kJ cm^{-3} and give rise to recoil pressures of several hundred MPa [27] (see Section 14.6.3 below).

The high volumetric energy density in the target material produced in Q-switched Er:YAG laser ablation results in a very large initial expansion velocity of the ablation plume that drives the emission of an equally fast shock wave. Shock front velocities are usually on the order of 2000–4000 m/s for both IR and UV wavelengths [27, 102–104], i.e., they reach values up to Mach 12. Measured shock wave and plume velocities correlate with the water content of the samples because lower water content results in smaller volumetric energy densities and less vigorous ablation. By contrast, the velocity of particulate fragments is larger for mechanically strong tissues (up to 1700 m/s for skin) than the velocity of droplets ejected in water ablation (up to 280 m/s) [27]. This is because the temperature required for thermal dissociation of the tissue matrix into volatile products is higher than the temperature required for complete vaporization of water. Therefore, tissue fragments become visible early in the ablation process when the ablation front has reached a depth at which the temperature is below the level required for thermolysis. At this time, the pressure driving the ejection is still very high. By contrast, droplet ejection starts only once the temperature at the ablation front has reached a lower level corresponding to the onset of a phase explosion. This results in smaller velocities for the droplet ejection.

The ablation plume exhibits complex dynamics. The plume expansion is nearly spherical during the initial phases of expansion but begins to propagate preferentially in the forward direction after 1–2 μs. For small radiant exposures, the interaction of the piston-like forward movement with the ambient air at rest results in ring vortex formation [27, 105]. For larger radiant exposures, a region of high density and pressure is created at the contact front between plume and surrounding air. The molecules and molecular clusters propagating with the plume possess a nonzero average velocity. When they collide with air molecules that are, on average, at rest, they are partially reflected back into the plume. As visible in Fig. 14.13, this reflection leads to the formation of an internal shock wave that begins to propagate toward the target surface when the rarefaction from the plume expansion has reduced the pressure in the plume considerably below its initial value [27, 106, 107]. The internal shock interacts with the particles and droplets of the plume and deforms the shape of the particle cloud during a time interval lasting about 10 μs. Due to the heating at the shock front, the passage of the internal shock wave through the reddish droplet cloud results in their vaporization.

The propagation of the shock front after a strong explosion in a homogeneous atmosphere was first theoretically described by Taylor [108] and Sedov [109, 110] and, using a higher order approximation, by Sakurai [111, 112]. These theories neglect the mass of the gas and debris driving the shock wave and are thus valid only once the shock wave has swept over a mass of atmospheric gas much greater than the mass in which the energy was initially concentrated. Various authors have later obtained solutions for the mass-dependent flow regime [113–115], and simple analytic solutions are available for some limiting cases. When the mass of the gas encompassed by the shock wave is much greater than the initial ablated mass and the pressure driving the shock is much greater than the atmospheric pressure ahead of the shock front, the position $R\,(t)$ of a spherical shock wave is governed by [116]

$$R(t) = \xi_1\,(E_0/\rho_0)^{1/5}\;t^{2/5} \tag{14.8}$$

and that of a planar shock wave such as emitted from a large irradiated spot size by [85]

$$R(t) = \xi_2\,(E_0/\rho_0)^{1/3}\;t^{2/3} \tag{14.9}$$

Here E_0 [J] is the energy driving the explosion, ρ_0 the density of the undisturbed gas, and $\xi_1[\mathrm{m}^{2/5}.\mathrm{kg}^{1/5}\cdot\mathrm{J}^{-1/5}\cdot\mathrm{s}^{-2/5}]$ and $\xi_2[\mathrm{kg}^{1/3}\cdot\mathrm{J}^{-1/3}\cdot\mathrm{s}^{-2/3}]$ are constants that depend on the specific heat capacity ratio γ of the gas. The peak pressure in the spherical case scales proportional to $E_0^{2/5}$ [110]. Once the shock wave pressure becomes comparable to the ambient pressure, its propagation is better described by the Jones' approximation [117, 118]. When the mass of the material removed is very large or the background pressure very low (including vacuum), the motion of a planar shock wave can be described by [119]

$$R(t) = \xi_3\,(E_0/M_0)^{1/2}\;t \tag{14.10}$$

where M_0 is the mass of the explosive debris. ξ_3 is a constant with dimensions $[\mathrm{m}^2 \cdot \mathrm{kg} \cdot \mathrm{J}^{-1} \cdot \mathrm{s}^{-2}]$. A comparison of experimental $R(t)$ data with Eqs. (14.8)–(14.10) allows an assessment of the transduction of laser pulse energy into blast wave energy E_0 [85, 118].

More refined numerical simulations by Brode [107] and the analytical treatment by Arnold and coworkers [106] include the spherical movements of the external shock front, the contact front between plume and ambient gas, and the internal shock front within the plume. Recently, Chen, Bogaerts and Vertes [120] presented a model for the propagation of the external shock wave propagation in atmospheric pressure laser ablation of water-rich targets that incorporates the nonlinear absorption of water and the phase explosion due to superheating. The model predicts a succession of an initially slow plume emission followed by a vigorously accelerated expansion, in good agreement with the experimental results of Apitz and Vogel [27] and the views presented above.

14.6.2 Primary Material Ejection in Microsecond Ablation

Free-running lasers typically provide pulse durations longer than 100 μs. Thus, unlike nanosecond ablation, plume formation and expansion occurs largely during the laser irradiation. As a result, the ablation plume influences the energy deposition of the laser radiation into the tissue target, and the plume dynamics is also influenced by the interaction of the laser beam with the ejected material. Nevertheless, the succession of a sub-ablative phase, development of a vapor plume, and material ejection is similar as with nanosecond pulses even though it occurs on a much longer time scale [121]. However, the heating rates available from microsecond laser pulses are generally much smaller than those available from nanosecond laser pulses of moderate to high radiant exposures. These lower heating rates are not sufficient to generate the temperatures necessary to dissociate molecules of the extracellular matrix and are only able to produce supercritical water at very large radiant exposures.

Free-running laser emission is characterized by intensity fluctuations during the laser pulse (“spiking” behavior). These intensity peaks modulate the vaporization and material ejection rates [101, 122] as well as the emission of acoustic transients generated during the ablation process [123, 124]. The intensity spikes of the laser pulse are coupled with the generation of individual transients as shown in Fig. 14.16.

The mechanisms leading to material ejection are the same as for nanosecond pulses: a phase explosion for mechanically weak materials and a succession of phase explosion and confined boiling for mechanically stronger tissues. Previously it was believed that the generation of a phase explosion requires very fast heating rates achieved only when using nanosecond pulses [32]. However, using time-resolved photography, Nahen and Vogel [121] demonstrated that a phase explosion can also be produced with laser pulses with duration on the order of 200 μs. This is shown in Fig. 14.17 that compares the ablation dynamics for Er:YAG laser irradiation of water, gelatin and skin using identical radiant exposures. The rapid droplet ejection during Er:YAG laser ablation of water that is observed after 40 μs can only

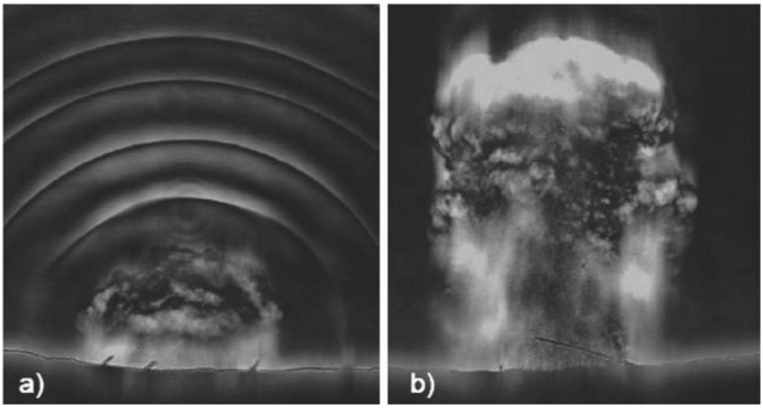

Fig. 14.16 Dark-field Schlieren images of the acoustic transients and ablation plume during skin ablation with a 200-µs Er:YAG laser pulse ($H = 20$ J/cm^2, spot size 2.3 mm) photographed (**a**) 22.4 µs and (**b**) 40 µs after the onset of the laser pulse. The images show acoustic transients arising from individual spikes in the free-running laser irradiation, and the plume containing vapor and tissue fragments. (Reprinted with permission from [99] with permission.)

be produced by a phase explosion because in the absence of stress confinement, no other mechanism gives rise to a material ejection perpendicular to the water surface. In gelatin, a phase explosion occurs at the same time as in water. However, the phase explosion only deforms the gelatin surface without rupturing it, and fracture of the gelatin surface and rapid particle ejection are observed only after a further pressure build-up through confined boiling (Section 14.4.5). The material ejection during skin ablation is also characterized by a phase explosion followed by confined boiling. However, the higher mechanical strength of skin causes a further delay of material ejection compared to gelatin. It is important to note that both for skin and gelatin targets fragments are ejected in the form of solid particles. The absence of droplet-like ejecta indicates that gelatin exposed to temperatures near the spinodal limit does not melt within of 200 µs, even though it melts at 60°C for sufficiently long heat exposures. This finding is consistent with the strong increase in denaturation temperature for very short exposures discussed in Section 14.2.

Initial material ejection velocities observed for microsecond laser ablation are roughly one order of magnitude lower than those reported for nanosecond ablation [125]. For free-running pulses, an increase of the radiant exposure results in an earlier onset of the material ejection but does not change the ejection velocity significantly. It is only for very large radiant exposures in which the first intensity spike of the free-running pulse provides a dose in excess of the ablation threshold that an increase of the ejection velocity is observed. By contrast, for nanosecond exposures an increase of the radiant exposure is always coupled with an increase of the volumetric energy density that translates directly into a higher temperature, pressure, and ejection velocity.

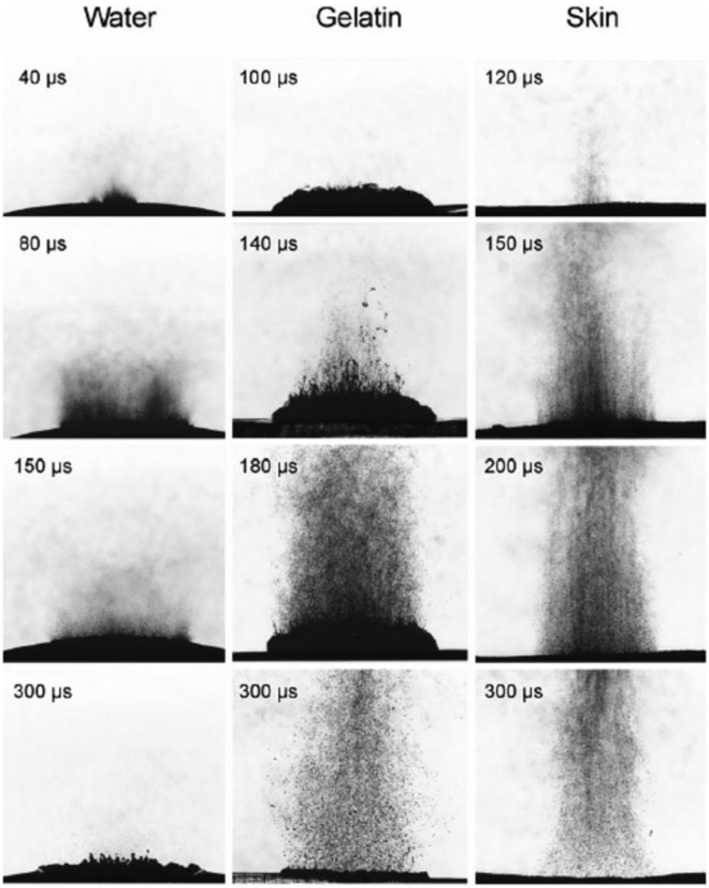

Fig. 14.17 Dynamics of Er:YAG laser ablation of water, gelatin with 70% water content, and skin using a radiant exposure of 4.6 J/cm^2, 5 mm spot size, and 200 µs pulse duration. The times after the beginning of the laser pulse when the photographs were taken are indicated on the individual frames. Note the increasing delay in the ejection of particulate matter with increasing mechanical strength of the target. (Reprinted with permission from [121] and [1].)

In both Q-switched and free-running laser ablation of soft tissues, material ejection continues for a considerable time following laser irradiation that can last up to several milliseconds [101–103, 105, 121, 126]. In general, post-pulse ablation lasts longer for mechanically weaker tissues, larger radiant exposures, and larger laser beam diameters. One possible driving force for the continuation of the ablation process after the end of the laser pulse is the heat retained in the tissue. A progressive weakening of the tissue matrix through thermal denaturation enables a propagation of the ablation front until the vapor pressure in the residual tissue drops below the ultimate tensile strength of the weakened tissue matrix. Another very important source of post-pulse ablation are hydrodynamic phenomena such as recoil stress-induced material expulsion.

14.6.3 Recoil Stress and Secondary Material Ejection

Both the rapidly expanding vapor plume and the ejected particles generate recoil stresses that impart momentum to the tissue. The linear momentum per unit area of the ablated material l [Pa·s] is the time integral of the recoil stress σ_{rec} [Pa] at the target surface

$$l = \int_0^\infty \sigma_{\text{rec}}(t)dt \tag{14.11}$$

A derivation of the peak recoil stress requires assumptions on the nature and duration of the ablation process. Various authors have presented solutions for the peak stress amplitude produced by a continuous vaporization process [31, 57, 127, 128], and by explosive ablation where the entire laser pulse is deposited prior to the onset of material removal [32, 129].

Experimental values for the recoil stress produced by nanosecond laser ablation have been obtained through direct pressure measurements using piezoelecteric transducers [31, 32, 130, 131], and, for water ablation, through analysis of the speed of the recoil-induced shock wave [27]. Peak pressures range from a few MPa at the ablation threshold up to several hundred MPa for radiant exposures well above threshold. For free-running microsecond laser pulses, average stress values during the laser irradiation have been determined through measurement of the recoil momentum using the ballistic pendulum method [56, 128], while the peak stress amplitudes produced by the intensity maxima of the free-running pulses, was obtained via transducer measurements [131]. Peak values of recoil stress produced during cornea ablation using free-running Er:YSSG laser irradiation at a radiant exposure of 50 J/cm^2 amounted to 2 MPa [131], while the average pressure value for skin ablation at the same radiant exposure was only 0.3 MPa [128].

In stress-confined tissue ablation, the compressive recoil stress transient is superimposed on a bipolar thermoelastic transient [132]. Figure 14.18 demonstrates the transition from a bipolar stress transient for radiant exposures below the ablation threshold to a monopolar compressive transient when the ablation threshold is exceeded. This transition and the corresponding increase in peak pressure is a sensitive method for the determination of the ablation threshold [31, 32, 130].

The recoil stress produced by both vaporization and material ejection in the primary ablation phase can induce a secondary material expulsion process that leads to a strong increase of the ablation efficiency [27, 127]. Recoil-induced material expulsion is most pronounced during ablation of liquids and mechanically weak tissues. Material will be ejected whenever the recoil stress component in the radial direction exceeds the mechanical strength of the tissue, as illustrated in Fig. 14.19.

The sequence of primary material ejection and recoil-induced material expulsion is shown in Fig. 14.20 for free-running and Q-switched Er:YAG laser ablation of liver. While the primary material ejection visible at short delay times takes place across the entire ablation area, recoil-induced expulsion occurs preferentially at

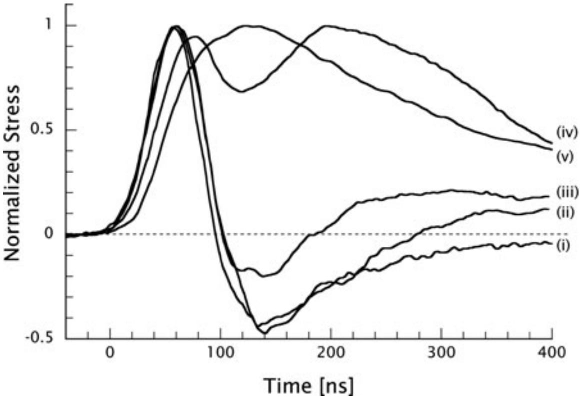

Fig. 14.18 Stress transients resulting from TEA CO_2 laser ($t_p = 30$ ns) irradiation of porcine dermis for radiant exposures below (i), at (ii), and above (iii)–(v) the ablation threshold. Radiant exposures below threshold produce bipolar thermoelastic stress transients. For radiant exposures equal to and above threshold, a compressive pulse is produced by the ablative recoil. (Adapted from [32] with permission. Copyright 1996 Biophysical Society)

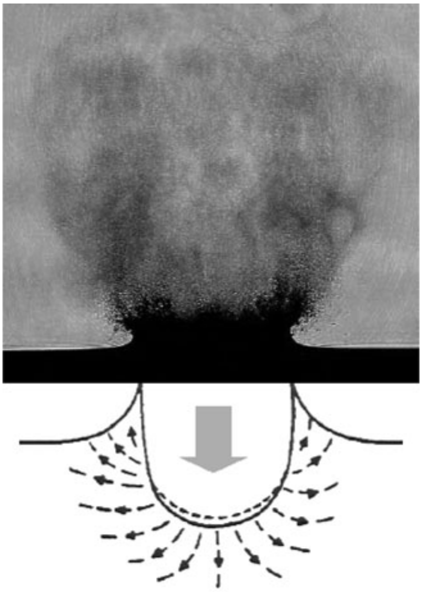

Fig. 14.19 Recoil-induced material expulsion in water ablation by 200-µs Er:YAG laser pulses, together with a schematic illustration showing the pathlines of the ejected material fragments. The lateral component of the recoil-induced flow collides with the surrounding fluid that is at rest, thus producing an upward directed splash

the ablation crater rim and includes the ejection of tissue fragments much larger than those ejected during the initial phase explosion. The recoil-induced ejection dynamics resembles the surface indentation and subsequent "splash" produced by the impact of liquid droplets on bulk liquids that has already been investigated in considerable detail [133, 134]. The mass expelled at later times far exceeds the

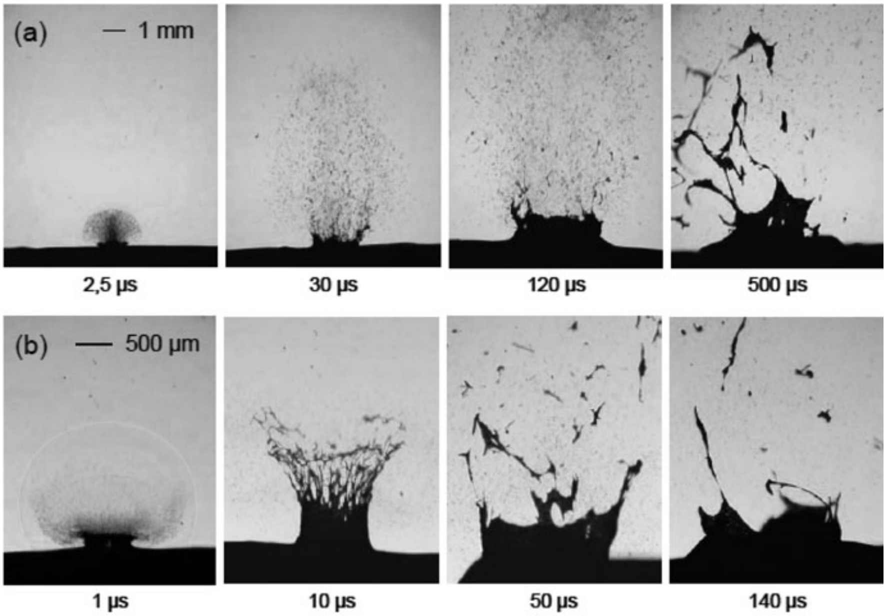

Fig. 14.20 Recoil-induced material expulsion for liver ablation by (**a**) 200-µs Er:YAG laser pulses at 100 J/cm^2 radiant exposure and 1.1 mm spot size, (**b**) 70-ns Er:YAG laser pulses at 5.4 J/cm^2 radiant exposure and 0.5 mm spot size. The primary material ejection produced by the phase changes in the target is also visible all images of (**a**) and in the first image of (**b**)

mass ejected during the primary ablation phase. However, the velocity of the ejecta is considerably slower.

Recoil-induced material expulsion begins after the primary ejection process, requires a radiant exposure well above the ablation threshold, and provides an increase of the ablation efficiency. A marked increase of the ablation efficiency at a certain radiant exposure has been observed for weak tissues as liver and myocardium as well as for gelatin with high water content but not for tissues with greater mechanical strength such as skin [27, 135]. Remarkably, no recoil-induced ejection was observed in skin ablation using Q-switched Er:YAG laser pulses even when the recoil stress was about 50 times larger than the quasi-static ultimate tensile strength of skin [2]. To understand this discrepancy, we must first consider that the recoil-induced tensile and shear stresses that contribute to tissue fracture may be considerably smaller than the measured compressive recoil stress. Moreover, the dynamic tensile strength of tissue at the extreme strain rates produced in pulsed laser ablation is much higher than the quasi-static values for the ultimate tensile strength found in the literature [15–17] (see Section 14.2). Finally, tissue fracture will only occur at sufficiently large strain that may not be achieved by stress transients of very short duration [1, 136, 137].

Figure 14.21a demonstrates that for mechanically weak tissues, the recoil-stress-induced material expulsion produces craters with a depth much larger then

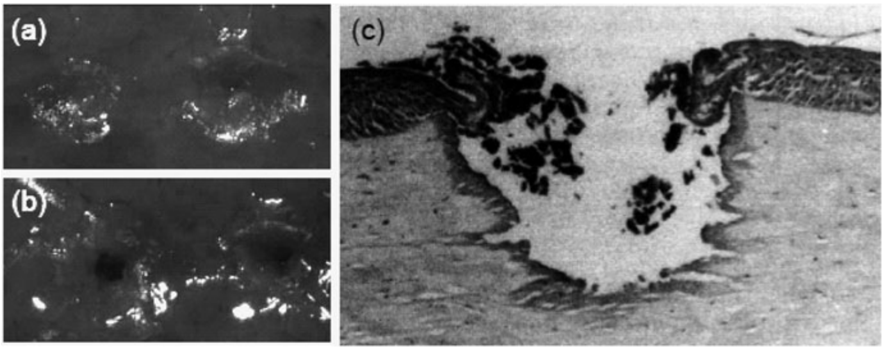

Fig. 14.21 (**a**) Crater produced during liver ablation by a 200-μs Er:YAG laser pulses of 32 and 50 J/cm^2 radiant exposure (2.5 and 1.6 mm spot size, respectively). (**b**) Histologic slide showing an ablation crater in bovine cornea produced by an Erbium:YSGG laser pulse with $t_p = 250$ μs and $H = 100$ J/cm^2. The tissue around the ablation crater exhibits a 25–50 μm zone of thermal damage (dark) and mechanical tearing between the corneal lamellae. ((**b**) Reprinted with permission from [128])

the optical penetration depth and a diameter much larger than the irradiated spot size. For mechanically strong tissues, the recoil stress does not lead to material expulsion. However, it can produce tissue tearing at the sides of the ablation crater as seen in Fig. 14.21b. The cracks and tearing patterns arise preferentially along morphological structures with reduced mechanical strength such as the transitions between corneal lamellae, sinusoid spaces holding blood between plates of cells in liver tissue, and their orientation is also influenced by the weakness of the longitudinal strength of blood vessels compared to their circumferential strength [128]. Tissue tearing at the rim of ablation craters was not observed for skin due to its 3-dimensional collagen network that can bear mechanical loads in an isotropic fashion.

Recoil-induced stress transients can also produce more subtle forms of collateral tissue damage further from the irradiation site. ArF-excimer ($\lambda = 193$ nm) laser ablation of skin may create epidermal and dermal photoacoustic damage [138, 139]. The recoil stress wave produced during ArF-excimer laser ablation of the cornea is focused into the eye ball and, due to diffraction, transformed into a bipolar shape with a tensile stress amplitude of up to 3.5 MPa [140]. Könz and coworkers [131] demonstrated recoil-induced damage of the corneal endothelium after mid-IR laser ablation of the corneal stroma that was due to the tensile stress generated upon partial reflection of the compressive recoil stress transient at the cornea-aqueous interface.

Thus, to achieve precise and gentle tissue ablation it is not sufficient to simply select a laser wavelength with small optical penetration depth and a pulse duration providing thermal confinement. In addition, one must avoid the production of extensive recoil stresses that may degrade the quality of the ablated surface and/or induce collateral mechanical damage. This restriction imposes an upper limit for the incident radiant exposure.

14.6.4 Shielding and Flow-Induced Material Redeposition

Absorption, scattering, and diffuse reflection of incident laser light by the ablation plume leads to a reduction of the energy delivered to the target tissue and a reduction of the ablation efficiency. Direct measurements of the diffuse reflectance of the plume [141] and of the entire reduction of optical transmission through the plume [121] provided values of the extinction coefficient within the plume produced by soft tissue ablation using Er:YAG laser irradiation ($\lambda = 2.94\,\mu\text{m}$, $t_p = 200\,\mu\text{s}$) on the order of 1 cm^{-1} [121].

Shielding is strongly enhanced when a series of pulses is applied instead of single pulses [141]. For skin ablation by means of Er:YAG laser pulses ($t_p \approx 300\,\mu\text{s}$) irradiating a spot of 2 mm diameter, Kaufmann and Hibst [142] observed a decrease of the etch depth per pulse from 40 to 10 µm when the pulse repetition rate was increased from 1 to 10 Hz. The reduction of the ablation efficiency was attributed to increased shielding by the ablation plume. When a considerably smaller spot size is used, the lateral spread of the plume removes a larger fraction of the ablation products out of the beam path, and the etch depth does not decrease with increasing repetition rate [143].

At very high radiant exposures, plasma formation in front of the target may lead to a further decrease of the optical transmission to the target [27, 105, 126] as illustrated in Fig. 14.22. Plasma formation starts at the target surface but the plasma grows rapidly after ignition into the space in front of the target surface, which results in very efficient shielding.

When radiant exposures close to the ablation threshold are used, the plume acquires a mushroom-like shape that exhibits a ring vortex at its top, a thin stem

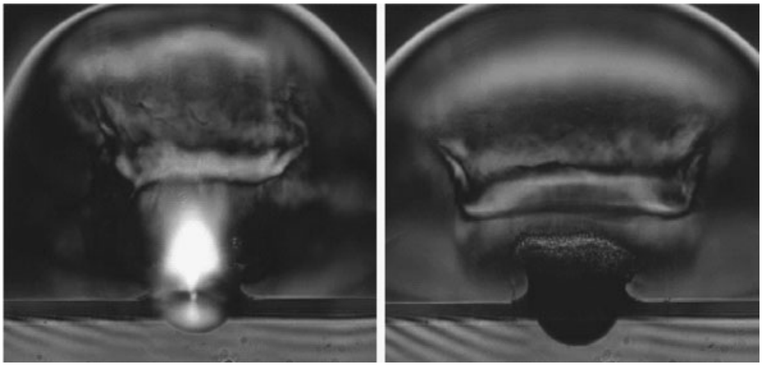

Fig. 14.22 Dark field images of water ablation at 5.4 J/cm^2 radiant exposure with and without plasma formation (0.5 mm spot size, image taken 2 µs after the laser exposure). The plasma originates in hot spots at the water surface and grows into the incoming laser beam. The recoil-induced cavity is considerably smaller in the case with plasma formation due to the "shielding" of the target by light absorption in the plasma. (Reprinted with permission from [27])

with a diameter smaller than the ablation spot and a radial flow component parallel to the surface at the foot of the plume [27, 105, 126]. The radial flow parallel to the tissue surface can result in a redistribution of ablation products across the ablation spot. For example, when performing corneal refractive surgery using large laser spot sizes, ablation rates were found to be smaller in the center of the ablation zone than in its periphery even though the irradiance was spatially homogeneous. As a result, "central islands" remained that distorted the intended refractive correction [145]. Photographic investigations of the plume dynamics revealed that the "central islands" are the result of a redeposition of ablated material after the end of the laser pulse that preferentially occurs near the stagnation point of the flow at the center of the ablated area [105]. A second factor contributing to the nonuniformity of the ablation rate is the attenuation of subsequent laser pulses in the center region of the ablated area by remnants of the plume from previous pulses that preferentially stay in the vicinity of the stagnation point [105].

14.7 Ablation Models and Metrics

In the previous sections we established that pulsed laser ablation always consists of a sequence of different phase transition processes that occur during and after laser irradiation. Moreover, we have shown that the initial primary material ejection is often followed by a secondary, recoil-induced ejection. The type and vigor of the phase transition and ejection processes during an individual ablation event depend on both the laser irradiance and radiant exposure as well as on the optical and mechanical tissue properties. Thus, it is impossible to formulate a simple comprehensive ablation model that describes these different aspects of the ablation process. Nevertheless, it is useful to formulate simplified models that elucidate basic features of the ablation behavior and parameter dependencies for specific ablation regimes. Particularly useful are models that illustrate the ablation behavior in extreme cases such as the "steady state" model for long laser pulses and the "blow-off" model for very short pulses. As long as one keeps the limitations of these models in mind, they can provide useful guidelines to interpret experimental data and to select laser parameters for an intended ablation outcome.

In this section, we first introduce common metrics that characterize the ablation process such as the threshold, enthalpy, and efficiency of ablation. We then describe the heuristic blow-off and steady-state models that use these metrics to predict ablation rates without reference to mechanistic aspects of the ablation process. In the next step, we discuss models that link the ablation outcome to underlying mechanisms. Models have not yet developed to the stage where they can address the full complexity of phase transitions and ejection mechanisms. Nevertheless, the models have provided insight into specific aspects of the ablation dynamics and the resulting collateral damage. Finally, we briefly describe the molecular dynamics approach that provide a microscopic view of the inception and dynamics of the ablation process.

14.7.1 Ablation Metrics

The *ablation threshold* H_{th} [J/cm^2] represents the minimum incident radiant exposure required to achieve ablative material removal. Molecular dynamics simulations and experiments show that radiant exposures below the ablation threshold results in thermal desorption of individual molecules while exposures above the ablation threshold produce volumetric ejection of large molecular clusters [93, 146, 147]. Thus, the ablation threshold is defined as the incident radiant exposure necessary to achieve *volumetric* ejection of tissue.

Perhaps the simplest means to determine the ablation threshold is to determine the radiant exposure at which the extrapolation of data for material removal or etch depth vs. incident radiant exposure intersects the abscissa, as indicated in Fig. 14.23 [144]. However, this approach may be inaccurate due to a lack of measurement sensitivity at radiant exposures close to the ablation threshold. A more sensitive, albeit indirect, measurement of ablation threshold has been obtained using piezoelectric transducers to measure the appearance of recoil stresses connected with material removal [31, 32, 130, 148]. High-speed photography has provided a sensitive and direct determination for the onset of material removal during pulsed laser irradiation [27, 121, 149], as shown in Figs. 14.13, 14.16 and 14.17. These measurements, when combined with the time-resolved recording of the laser irradiance, can provide an accurate measurement of the threshold radiant exposure.

The *ablation enthalpy* h_{abl} [J/kg] or heat of ablation is often used to describe the energetics of ablation [1, 135]. As depicted in Fig. 14.23, ablation enthalpy is a differential quantity that varies with the incident radiant exposure and represents the incremental amount of laser energy required to ablate an additional mass of tissue. We shall see that steady-state models invoke a constant ablation enthalpy that can be determined by fitting a line to etch depth vs. incident radiant exposure data and taking the reciprocal of the slope of this line. In the blow-off model the ablation enthalpy increases monotonically with radiant exposure.

Ablation efficiency η_{abl} [kg/J] is a metric for the total energy necessary to remove a given mass of tissue (Fig. 14.23). Ablation efficiency decreases with

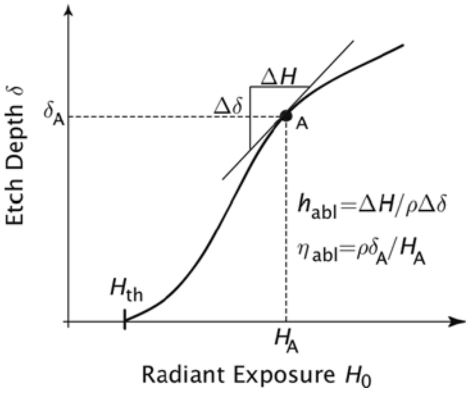

Fig. 14.23 Graph depicting the relationship between etch depth and radiant exposure for a hypothetical tissue ablation process to illustrate the concepts of ablation threshold H_{th}, ablation enthalpy h_{abl}, and ablation efficiency h_{abl}

increasing ultimate tensile strength (UTS) of tissue and increases with radiant exposure [27, 150]. For tissues with high UTS, such as skin and aorta, the ablation efficiency reaches a maximum at radiant exposures several times the ablation threshold and remains roughly constant while, for liver, a very weak tissue, the ablation efficiency continues to increase even for radiant exposures 10 times larger than the ablation threshold [27, 150]. The continued increase in ablation efficiency is due to the susceptibility of mechanically weak targets to recoil-induced material removal (Section 14.6.3).

14.7.2 Heuristic Models

Blow-off Model. The blow-off model was first developed to predict the etch depth resulting from nanosecond UV laser ablation of polymers [69, 151] and has also been applied to tissue ablation. This model is based on four assumptions. First, the Lambert-Beer law accurately describes the spatial distribution of absorbed laser energy in the tissue. Second, a threshold radiant exposure H_{th} is required for the initiation of ablation and lower radiant exposures result only in heating of the target. Third, material removal commences only after the end of the laser irradiation. Fourth, the conditions for thermal confinement are satisfied. Thermal confinement is nearly always achieved when performing laser ablation using pulse durations of 100 ns or less. The distribution of the volumetric energy density within the target immediately after the end of the laser pulse is then described by $W(z) = \mu_a H_0 \exp(-\mu_a z)$. For incident radiant exposures H_0 larger than the threshold radiant exposure H_{th}, all material receiving a radiant exposure in excess of H_{th} is removed. This results in a semi-logarithmic relationship between the etch depth δ [m] and the incident radiant exposure:

$$\delta = \frac{1}{\mu_a} \ln \left(\frac{H_0}{H_{th}} \right) \tag{14.12}$$

The use of laser wavelengths at which the tissue absorption coefficient is large results in a low threshold radiant exposure. As illustrated in Fig. 14.24a, the superficial penetration of laser radiation results in small etch depths that increase slowly with radiant exposure. By contrast, small tissue absorption coefficients result in much larger threshold radiant exposures, and the deeper optical penetration produces a much steeper slope of the etch depth vs. radiant exposure curve. These predictions of the blow-off model (Fig. 14.24a) are corroborated by a comparison with experimental data for 193 and 248 nm pulsed excimer laser ablation of cornea shown in Fig. 14.24b [152, 153].

Steady-State Model. For microsecond laser pulses, material removal typically occurs during irradiation of the target. Such processes can be modeled by assuming that a fixed amount of energy is required for removal of a unit mass of tissue, i.e. h_{abl} [J/kg] is constant. This is adequate to describe a continuous ablation process in which the resulting rate of material removal balances the irradiance delivered to the tissue. It is also assumed that material removal begins soon after the beginning of laser irradiation and continues during the entire laser pulse. For doses in excess of the ablation threshold, the steady-state model predicts a linear relationship between the etch depth and incident radiant exposure. The slope of the etch depth and incident radiant exposure curve depends solely on the ablation enthalpy h_{abl} as:

$$\delta = \frac{H_0 - H_{\mathrm{th}}}{\rho\ h_{\mathrm{abl}}} \tag{14.13}$$

where h_{abl} is assumed to be constant. Note that there is no explicit dependence of the etch depth on absorption coefficient and there is a direct proportionality between the threshold radiant exposure and ablation enthalpy, namely, $H_{\mathrm{th}} = \rho h_{\mathrm{abl}}/\mu_{\mathrm{a}}$.

Comparison of Blow-off and Steady-State Models. To predict material removal, heuristic models require as input the optical absorption coefficient and either the

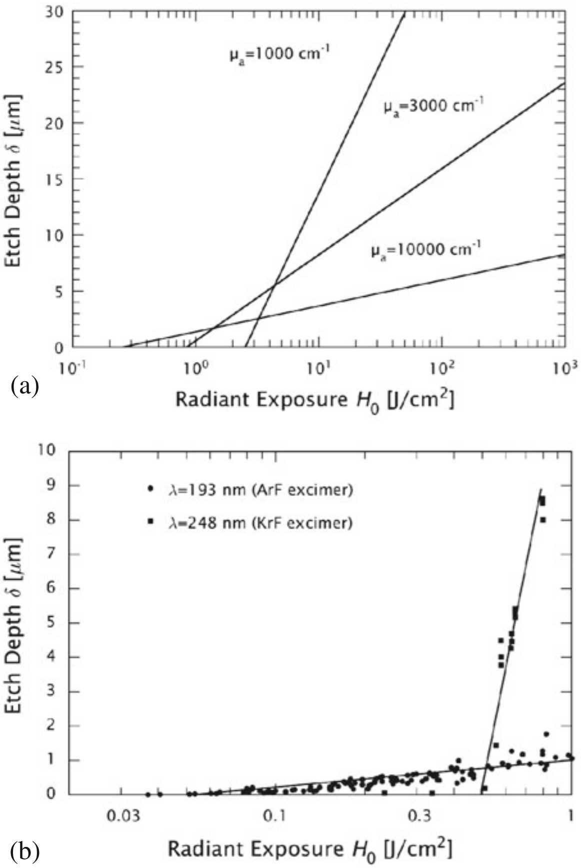

Fig. 14.24 (**a**) Predictions for etch depth vs. radiant exposure given by the blow-off ablation model for three different absorption coefficients and constant volumetric threshold energy density $W_{\mathrm{th}} = 2530$ J/cm^3 which is the sum of the sensible and latent heats for the vaporization of water. (**b**) Etch depth vs. radiant exposure data for ArF- and KrF-excimer laser ablation of cornea where $\mu_{\mathrm{a}} = 29000$ and 290 cm^{-1}, respectively. Data are compiled from [152] and [153]

threshold radiant exposure (blow-off model) or the ablation enthalpy (steady-state model). It is instructive to compare predictions of both models with respect to ablation efficiency. The ablation efficiency η_{abl} [kg/J] is defined as the amount of mass removed per unit energy delivered to the tissue and given by:

$$\eta_{\mathrm{abl}} = \frac{\rho\delta}{H_0} \tag{14.14}$$

Substituting Eqs. (12) or (13) into Eq. (14) provides expressions for the ablation efficiency predicted by the blow-off and steady-state models, respectively:

$$\eta_{\mathrm{abl}} = \frac{\rho}{\mu_a H_0} \ln\left(\frac{H_0}{H_{\mathrm{th}}}\right) \text{(blow-off)} \tag{14.15}$$

$$\eta_{\mathrm{abl}} = \frac{H_0 - H_{\mathrm{th}}}{h_{\mathrm{abl}} H_0} \text{(steady-state)} \tag{14.16}$$

For both blow-off and steady-state models, the ablation efficiency is zero at the threshold radiant exposure because a finite amount of energy is expended without any material removal. Also, in both models, a constant threshold energy density, $\mu_a H_{\mathrm{th}}$, results in a maximum ablation efficiency that is independent of the optical absorption coefficient. In the blow-off model, the ablation efficiency reaches a maximum at an incident radiant exposure of approximately $2.7H_{\mathrm{th}}$ and decreases monotonically at larger doses (see Fig. 33 in Ref. [1]). Thus for large radiant exposures much of the laser energy is poorly utilized by "overheating" superficial tissue layers far in excess of that required for their removal. In the steady state model, the ablation efficiency increases monotonically and asymptotically approaches a value $\eta_{\mathrm{abl}} = 1/h_{\mathrm{abl}}$ for $H_0 >> H_{\mathrm{th}}$.

Hibst unified blow-off and steady state ablation models within a single framework to accommodate the effects of plume absorption on the ablation process [125]. This framework reduces to the steady-state model for cases where the ablation plume is transparent to the incident radiation and to the blow-off model for a steady-state process where the ablation plume possesses an absorption coefficient identical to the tissue. Defining $\gamma = (\mu_{a,p}/\mu_p)$ where $\mu_{a,p}$ and μ_a are the optical absorption coefficients of the plume and tissue, respectively, Hibst showed that the etch depth δ is given by:

$$\delta = \frac{1}{\mu_a \gamma} \ln\left(\gamma \frac{H_0}{H_{th}} - \gamma + 1\right) \tag{14.17}$$

Predictions equivalent to that of the steady-state and blow-off models are recovered for $\gamma \rightarrow 0$ and $\gamma \rightarrow 1$, respectively, and are shown for different values of γ in Fig. 14.25.

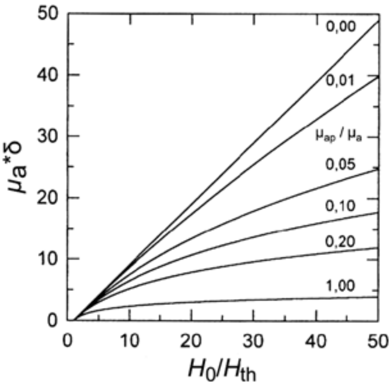

Fig. 14.25 Predictions for the variation of normalized etch depth with normalized radiant exposure predicted an ablation model that considers optical absorption associated by the ablation plume. Results are shown for various ratios for the optical absorption coefficient of the plume relative to the tissue. (Reprinted with permission from [125])

14.7.3 Mechanistic Models

The high degree of abstraction from physical ablation mechanisms that characterize heuristic models is a strength because it enables the description of different types of ablation processes as long as the model assumptions are fulfilled on a phenomenologic level. However, it is only when ablation mechanisms are explicitly considered that the origins of collateral effects can be identified and their spatial extent predicted.

Steady-state Vaporization Models. The first generation of mechanistic models developed in the 1980s and 1990s treated ablation as a rapid surface vaporization or boiling, considering thermal diffusion [43, 154–159]. The predictions of these models for threshold radiant exposure and material removal did not agree very well with experimental data because the models neglect explosive types of primary phase transitions, ignore the modification of all phase transitions by the tissue matrix, and they do not consider recoil-induced secondary material ejection. However, they provided estimates of the extent of thermal injury resulting from ablation and thus led to the discovery that thermal injury can be considerably reduced by using high laser irradiances that remove tissue at a speed faster than that associated with thermal diffusion [43, 156].

Thermo-mechanical Models. The first comprehensive attempt at integrating thermomechanical processes into a steady-state model of tissue ablation was made by Zweig, Frenz and co-workers starting in the late 1980s [56, 57, 160]. In this model, it is postulated that tissue can undergo two phase change processes: (a) a transition from a solid to liquid phase within the tissue bulk and (b) a transition from a liquid to vapor phase at the tissue surface. The solid–liquid phase transition is assumed to occur upon thermal denaturation, at which point the tissue loses mechanical integrity and “flows” under the action of shear stresses or pressure gradients. This allows for lateral pressure gradients in the vapor plume to eject denatured tissue “liquid” and thus provides material removal at ablation enthalpies lower than the vaporization enthalpy for water. Unfortunately, this model has three major deficiencies. First, experimental evidence shows that tissue is not liquified during ablation but ejected in the form of fragments (Figs. 14.14 and 14.17). Second, the model does not consider phase explosions or confined boiling as driving the ablation process and thus neglects material ejection during the primary material removal process. Third, the mechanical component of ablation arises only as a by-product of pressure gradients in the ablation plume that are oriented *parallel* to the target surface, and the impact of recoil forces on material removal was neglected. The pressure gradients are assumed to originate from the radial variations of irradiance within a Gaussian beam that would result in radial variations of the vapor pressure in the plume. Zweig conceded that mechanical effects by the lateral vapor pressure gradients in the plume are relevant only for ablation using microsecond pulses and very small spot sizes because they "become insignificant if the liquid cannot transverse the irradiated spot during the laser pulse, as is typically the case for Q-switched pulses" [57]. However, he did not proceed to analyze the effects of the recoil pressure that provide a significant contribution to ablation, especially for nanosecond laser pulses [27].

A more realistic approach to describe the interplay between tissue matrix and phase transitions was taken by Majaron and co-workers who introduced the concept of confined boiling (see Section 14.4.5) [53]. Confined boiling was modeled by considering the thermodynamic behavior of tissue water when heated within an elastic tissue matrix. This was the first attempt at modeling explosive material removal as the primary process of tissue ablation. The model accurately predicts that explosive material removal can be initiated without supplying the entire vaporization enthalpy. Moreover it predicts, in agreement with experiment, that the threshold radiant exposure is weakly dependent on tissue stiffness but varies significantly with the ultimate tensile strength [150]. However, the model only examines the initiation of explosive material removal and does not consider the ablation process at radiant exposures larger than the ablation threshold. Furthermore, it does not consider phase transitions other than boiling.

Existing mechanistic models highlight only specific aspects of the ablation process but do not integrate the various phase transitions and secondary material removal processes involved to provide a comprehensive picture. The dynamics and interplay of both the phase transition processes and recoil induced effects depend on the spatio-temporal evolution of the volumetric energy density in the target as well as on the tissue properties. As a result of this complexity, the dependence between ablation depth and radiant exposure over a larger range of radiant exposures must be nonlinear. Thus any simple relationship between radiant exposure and ablation depth as predicted by heuristic and simple mechanistic models can only provide an approximate prediction over a limited range of radiant exposures. Within these limits, an assessment of the ablation rate and efficiency within the context of the heuristic blow-off or steady state models (Section 14.7.2), and an estimation of ablation thresholds and thermal damage zones based on mechanistic models is still valuable and remains in prevalent use. However, modeling of the sequence of continuous and explosive phase transitions in the primary ablation process and of recoil-induced material ejection will be required to obtain a mechanistically sound and reliable prediction of ablation depth and collateral damage. The development of such models thus represents an important challenge for future work.

14.7.4 Molecular Dynamics Simulations

With conceptual advances in modeling, as well as advances in computational power, molecular dynamics (MD) simulations are becoming a valuable approach for developing an understanding of ablation on the microscale [75, 97, 161–164]. Computational molecular dynamics offers predictions of the motion of molecular units produced by the deposition of laser energy. In these computations, macroscopic thermodynamic constraints are not imposed explicitly. Rather, ablation arises as a natural consequence of molecular interactions governed by the implementation of the equations of motion, intermolecular interactions, energy transfer, and molecular excitation within the model system.

The MD approach yields a wealth of information regarding the inception of phase transitions and the time-evolution of the size and velocity distribution of the ablation products that are difficult to obtain by other means. As an example, Fig. 14.26 provides the time evolution of a 2-dimensional system following the delivery of a 15 ps laser pulse with an incident radiant exposure two times the ablation threshold. These simulations reveal the volumetric nature of the ablative material removal process where small and large clusters leave the material bulk from locations not limited to those on the material surface. This is quite distinct from evaporative and desorption processes where material removal tends to occur strictly from the material surface

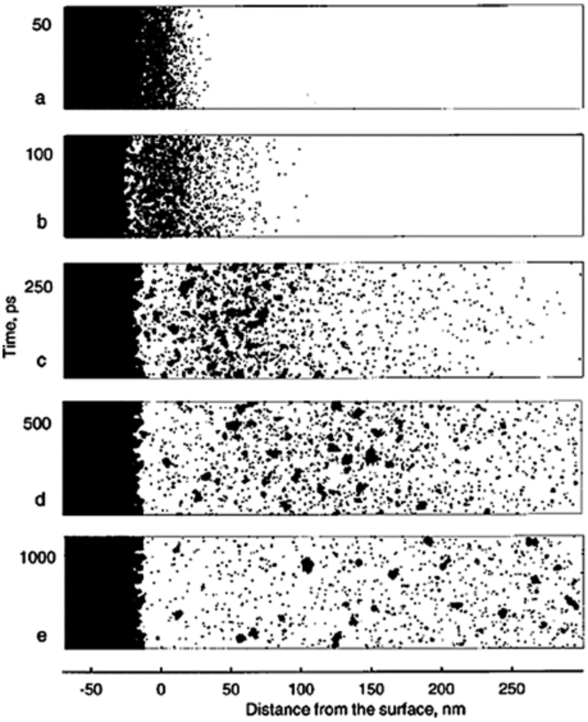

Fig. 14.26 Time development of an ablation plume for a 2D molecular dynamics simulation. The radiant exposure is roughly 2× the ablation threshold. The average energy deposited is 0.30 eV per particle in the irradiated region whereas the cohesive energy is 0.31 eV. The laser pulse width is 15 ps. (Reprinted with permission from [162])

and consists predominantly of single molecules. The MD approach has already provided valuable insights into the microscopic dynamics of desorption/ablation of both homogeneous and heterogeneous materials [165, 166] and is thus well suited to provide insights into the ablation dynamics of biological tissues. MD simulations are especially valuable for the analysis of stress-confined ablation processes because they are able to model the void formation and coalescence in heated and stretched materials [167, 168]. The main limitation of the MD approach are the very limited spatial and temporal scales that can be addressed.

14.8 UV and IR Ablation

The most common clinical application of pulsed tissue ablation is corneal refractive surgery using ArF excimer laser ($\lambda \approx 193$ nm) pulses of 20–30 ns duration. When ArF excimer laser pulses were first applied for the ablation of biological tissue, the smooth, precise, and nearly damage free character of the ablation [70, 152, 169–171] as shown in Fig. 14.27a was remarkable. This result seemed enigmatic in comparison to the much inferior ablation quality produced by hydrogen fluoride lasers ($\lambda = 3.0$ μm) [172, 173] or by Q-switched pulses from Er:YAG ($\lambda = 2.94$ μm) or Er:YSGG ($\lambda = 2.79$ μm) lasers [174], as shown in Fig. 14.27b because it appeared that the optical absorption coefficients at the two wavelength regions (190 nm vs. 2.8–3.0 μm) were comparable [170, 175]. Later this issue became even more perplexing when it was shown that a reduction in laser pulse duration from ≈ 50 ns to

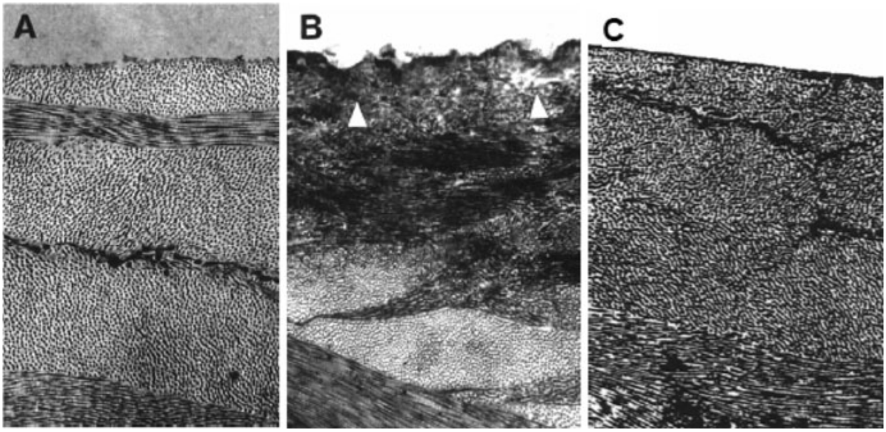

Fig. 14.27 Transmission electron micrographs of corneal ablation with (**a**) 193 nm ArF-excimer laser irradiation ($\lambda = 193$ nm), (**b**) Q-switched Er:YAG laser irradiation ($\lambda = 2940$ nm), and (**c**) 6-ns pulses from an optical parametric oscillator (OPO) emitting at 2.94 μm. Magnification 10000×. The damaged surface zone is visible as thin dark line in (**a**) and (**c**), and demarcated by arrowheads in (**b**). The damage zone has a thicknesses of ≤0.2 μm and in (**a**) and ≤0.3 μm (**c**), respectively, while it is 1–2 μm thick in (**b**) [176]

6 ns enabled 2.94 μm radiation to provide ablation quality similar to that of the ArF excimer laser (Fig. 14.27c) [176].

The common argument advanced to explain the differences between UV and IR ablation is that UV radiation induces photochemical processes which directly break chemical bonds, while IR laser ablation is governed solely by thermal processes. However, extensive investigations in the late 1980s and 1990s revealed that the actual picture is much more complex. As explained in Section 14.4.8, UV laser ablation is never an exclusively photochemical process, but involves an interplay of photochemical and photothermal processes. Moreover, for both UV and IR wavelengths, photomechanical mechanisms must be considered to fully understand the ablation dynamics and outcome. A detailed description of this picture and the underlying data are presented in the recent review article by Vogel and Venugopalan [1]; here, we will simply summarize the main findings.

Several studies using different measurement techniques [13, 153, 177] showed that the optical penetration depth of ArF excimer laser light is in the order of 0.25–0.5 μm rather than 3.7 μm as reported in the initial study [170]. In turn, mid-infrared spectroscopic studies of the temperature dependence of the optical absorption of water [10–12] revealed that the optical absorption of water drops significantly with temperature at both $\lambda = 2.94$ and 2.79 μm. While the optical absorption depth of water is 0.7 μm at room temperature, it exceeds 5 μm at radiant exposures $H_0 > 10\ \mathrm{J/cm^2}$ as shown in Fig. 14.2. Thus under ablative conditions the optical absorption coefficient of tissue at $\lambda = 193$ nm is actually about an order of magnitude larger than that in the $\lambda = 3$ μm region.

While the extremely small optical penetration depth explains the small etch depths and zones of thermal injury achieved by ArF excimer lasers, one must consider the role of photochemical effects, stress confinement, and heat transfer between tissue constituents to elucidate the differences in ablation dynamics and surface quality produced by UV and IR laser pulses of different durations. Table 14.1 provides a list of laser and tissue parameters relevant for this discussion. We use the ArF excimer laser ($\lambda = 193$ nm) and Q-switched Er:YSSG laser ($\lambda = 2.79$ μm) as examples for ablation without stress confinement, and the KrF excimer laser ($\lambda = 248$ nm) and an optical parametric oscillator (OPO) emitting radiation at $\lambda = 2.94$ μm as examples for ablation processes that are influenced by thermoelastic stresses. The table provides the pulse duration and tissue optical penetration depth for each laser source as well as the dimensionless pulse durations t_d^* and t_m^* that are normalized by the characteristic thermal diffusion and stress propagation times across the heated volume, respectively (see Section 14.3). Note that thermally confined conditions ($t_d^* \lesssim 1$) are achieved in all cases.

The volumetric energy density required for the onset of ablation is much smaller in cases with stress confinement, and increases as the degree of confinement decreases. When only thermal confinement is achieved, the threshold volumetric energy density for ablation resembles the energy density necessary to heat water from room temperature to the spinodal limit, which is 1270 J/cm^3 for pure water and 890 J/cm^3 for tissue with 70% water content. Thus it is considerably smaller than the vaporization enthalpy of water (2255 J/cm^3), which indicates the important role of material ejection for laser ablation.

Table 14.1 Wavelength λ, photon energy E_λ, pulse duration t_p, optical absorption depth μ_a^{-1}, dimensionless pulse durations t_m^* and t_d^* normalized by the stress propagation time and thermal diffusion time across the heated volume, respectively, volumetric energy density at ablation threshold W_{th}, and width of thermal damage zone d for IR and UV laser ablation of tissue. For comparison, the volumetric energy densities necessary to heat water from room temperature to the spinodal limit and to produce complete vaporization are 1270 and 25855 J/cm^3, respectively

Laser	λ [nm]	E_λ[eV]	t_p[ns]	μ_a^{-1} [µm]	$t_m^*(= \mu_a c_a t_p)$	t_d^* $(= \kappa \mu_a^2 t_p)$	H_{th}[J/cm^2]	S_{th}[J/cm^3]	d [µm]
OPO	2940	0.42	6	1.5	6	3.5×10^{-3}	0.035	230	≤ 0.3
Q-sw Er:YSGG	2790	0.44	40	3	20	5.8×10^{-4}	0.24	800	1–2 (Er:YAG)
KrF-excimer	248	5.0	34	30	1.2	3.5×10^{-6}	0.21	70	≈ 2
ArF-excimer	193	6.4	22	0.35	94	3.2×10^{-2}	0.050	1400	≤ 0.2

Data are compiled from [31] and [32], with the exception of the data for the thermal damage zones that are taken from [152] and [176].

With only thermal confinement, the thermal damage zone is similar to the optical penetration depth resulting in damage zones $\leq 0.2\ \mu\text{m}$ for ArF laser irradiation and 1–2 μm for Q-switched Er:YSSG laser irradiation. However, when stress confinement is provided in addition to thermal confinement, the thermal damage zone is much smaller than the optical penetration depth. Specifically, the width of the damage zone is only 1/20 of the penetration depth of KrF laser irradiation ($t_m^* = 1.2$, relatively strong stress confinement) and 1/5 of the penetration depth of the IR-OPO irradiation ($t_m^* = 6$, weak stress confinement). The influence of thermoelastic stresses is the key factor that explains how ablation with IR-OPO radiation at $\lambda = 2.94\ \mu\text{m}$ achieves a damage zone that is almost as small as that produced by the ArF excimer laser even though its optical penetration depth is significantly larger.

We saw above that the precision of ablation achieved by different UV and IR lasers can be explained in terms of the optical penetration depth and thermal and stress confinement. However, to understand experimental observations that UV ablation starts earlier and progresses more smoothly than IR ablation, one must consider in addition the influence of the tissue matrix on phase transitions in the tissue water and the role of photochemical decomposition of this matrix [1, 31, 32]. The time necessary for the onset of material removal represents the timescale required for tissue decomposition and can be inferred from measurements of the acoustic transients generated by recoil of the ablation products. For Q-sw Er:YSGG laser ablation, these measurements indicate that radiant exposures close to the ablation threshold result in an explosive onset of material removal that occurs towards the end of the laser irradiation [32]. By contrast, in ArF-excimer laser ablation stress transients due to ablative recoil begin promptly after the start of the laser pulse [31, 81, 82, 130, 178], and material removal proceeds continuously during the irradiation [31]. This result is consistent with the finding that the ejection velocity of plume material produced by ArF excimer laser ablation ($v = 600$ m/s for cornea ablation using $H_0 = 0.3 = 1\ \text{J/cm}^2$) is much smaller than that for Q-sw Er:YAG ablation at similar volumetric energy density within the target tissue ($v \approx 1400$ m/s for skin ablation using $H_0 \approx 25\ \text{J/cm}^2$) [27, 101, 102, 126].

Both the different timing of the onset of material removal and the different ejection velocities can be traced back to different decomposition kinetics of the tissue matrix. For IR laser irradiation at radiant exposures similar to the ablation threshold, the mechanical integrity of the tissue matrix is essentially maintained during the laser pulse (Fig. 14.17b, c) and ablation occurs only after the tissue matrix has been ruptured via phase explosion or confined boiling. This scenario explains the explosive character of the ablation dynamics and the rough surface of the ablation crater produced by Q-switched Er:YSSG irradiation (Fig. 14.27b). By contrast, the more rapid onset of the recoil stress in UV ablation suggests that the tissue matrix is destroyed more rapidly than in IR ablation. Thermal denaturation cannot be used to explain the early degradation of the tissue matrix in UV ablation because a similarly rapid onset would then also be produced by IR exposures as the heat transfer between tissue water and collagen fibrils occurs on a nanosecond time scale (see Section 14.2 and Eq. (14.2)). Photochemical decomposition is much more likely to be responsible for rapid degradation of the tissue matrix during UV laser irradiation. However, this does not imply that photochemical decomposition is the only mechanism relevant for UV ablation. In ArF-excimer laser ablation, the peptide bond linking the amino acids serves as the primary absorber. Several authors have shown that although a considerable fraction of the chemical bonds present in the tissue matrix is affected by photochemical decomposition [89, 94, 178] this fraction is insufficient to drive ablation by purely photochemical dissociation [92, 93]. To obtain a complete picture of all driving forces, one needs to include the phase transition of the tissue water. Thermal diffusion from the collagen heats the water to temperatures >> 100°C on a nanosecond time scale, which in turn promotes direct absorption of 193-nm laser light by water at elevated temperatures [1, 13, 179]. Thus ArF-excimer laser ablation is likely driven by a combination of photochemical and photothermal mechanisms. Photochemical effects are primarily responsible for tissue matrix decomposition and weakening that greatly reduces the explosive character of the ablation process while the photothermal processses are involved in the ejection of the fragments.

ArF-excimer laser ablation of tissue is less violent than IR laser ablation of either tissue or pure water which does not have a structural matrix. In IR laser ablation of water, the material ejection is driven by a phase explosion of superheated water or a vapor explosion of supercritical water that occurs mainly towards the end of the laser pulse [27]. By contrast, in ArF-excimer laser ablation, it is likely that the volatile gaseous products of the photodecomposition process produced during the heating of the tissue water serve to avert a phase explosion. A variety of organic gases including NH_2, C_2H_2, CH_2NH_2, and CO_2 in addition to water vapor have been found in the plume produced by 193-nm and 248-nm ablation of corneal tissue. [180] The volatile photodecomposition products provide a large number of boiling nuclei that promote a vaporization process and lower the degree of superheating in a way that prevents the spinodal limit from being reached. Analogous to a confined boiling process (Section 14.4.5), ablation will probably occur when the pressure from the volatile dissociation products, together with the vapor pressure from the heated tissue water, exceeds the tensile strength of the tissue matrix. However, since the strength of the matrix is strongly reduced by photochemical processes, the ablation process is less explosive than in IR ablation driven by a phase explosion.

It is interesting to note that the volumetric energy density at the ablation threshold is higher when using the ArF-excimer laser as compared to the Er:YSGG laser (Table 14.1). While the photochemical contribution to UV ablation changes the dynamics of tissue ablation, it does not reduce the ablation threshold such as predicted for photochemically enhanced ablation of organic solids [97]. The high ablation threshold correlates with findings that a large fraction of the tissue matrix is transformed into gaseous products [181] and that particulate ejecta of ArF laser ablation plumes [102, 105, 126] are much smaller than those produced by Q-switched IR laser tissue ablation close to the ablation threshold [27]. The photochemical decomposition of tissue into gaseous products and small particles requires more energy than the partial vaporization of tissue water and ejection of large tissue fragments produced by a phase explosion. By contrast, when photochemical weakening of the tissue matrix arises in conjunction with the generation of thermoelastic tensile stresses (for example in KrF excimer laser ablation), ablation is associated with the ejection of large particles [126], and the volumetric energy density required for ablation is dramatically lowered (Table 14.1).

14.9 Ablation in a Liquid Environment

Ablation in a liquid environment is most often encountered when delivering laser radiation through optical fibers for medical applications inside the human body. Current technology places significant limits on the use of optical fibers to transmit the laser wavelengths most suitable for precise tissue ablation in air: $\lambda = 193$ nm (ArF-excimer), 248 nm (KrF-excimer), 2.79 μm (Er:YSSG), 2.94 μm (Er:YAG), and 10.6 μm (CO_2). Therefore, wavelengths that are well transmitted through low-OH quartz fibers e.g., $\lambda = 308$ nm (XeF-excimer), 2.01 μm (Cr:Tm:YAG), and 2.12 μm (Cr:Tm:Ho:YAG), are most often used for ablation in liquid environments. While these wavelengths are not as highly absorbed by protein or water, (see Fig. 14.2a), their optical penetration depth is still fairly small: $\approx$50 μm for $\lambda = 308$ nm [182, 183], $\approx$170 μm for $\lambda = 2.01$ μm (thulium laser), and $\approx$350 μm for $\lambda = 2.12$ μm (holmium laser), respectively [184].

In a liquid environment, a layer of aqueous fluid is usually present between the tip of the optical fiber and the tissue surface. This fluid absorbs all the IR laser wavelengths listed above and thus needs to be ablated or displaced before the radiation can reach the tissue surface and tissue ablation can start. A similar problem is encountered during UV ablation if the fluid is blood, due to UV absorption by hemoglobin (see Fig. 14.2a). However, once the radiation is delivered to the tissue, the kinetics of the phase transitions in the liquid environment are similar to those in a gaseous environment, with the exception that surface vaporization plays no role. As a result, ablation thresholds, as measured by the deposited volumetric energy density are almost the same in liquid environments as those observed in air [67, 130].

The most characteristic feature of ablation in a liquid environment is the confinement of the ablation products by the liquid. Therefore, ablation in a liquid environment is accompanied by bubble formation and much stronger mechanical effects than observed in a gaseous environment [1]. The expansion of gaseous products produced during tissue ablation creates a bubble in the liquid surrounding the ablation site. When the optical fiber is not in contact with tissue, a bubble is also formed by absorption of laser radiation in the liquid separating the fiber tip and the tissue surface, as shown in Fig. 14.28a. This bubble is essential for the transmission of optical energy to the target, and the mechanisms governing its formation and subsequent dynamics have received much attention by researchers [182, 185–192].

Experiments have demonstrated bubble formation at the tip of an optical fiber at volumetric energy densities smaller than the vaporization enthalpy of water at constant pressure [186, 187, 193]. This observation of “partial vaporization” has puzzled some researchers but can be easily explained by examining the kinetics

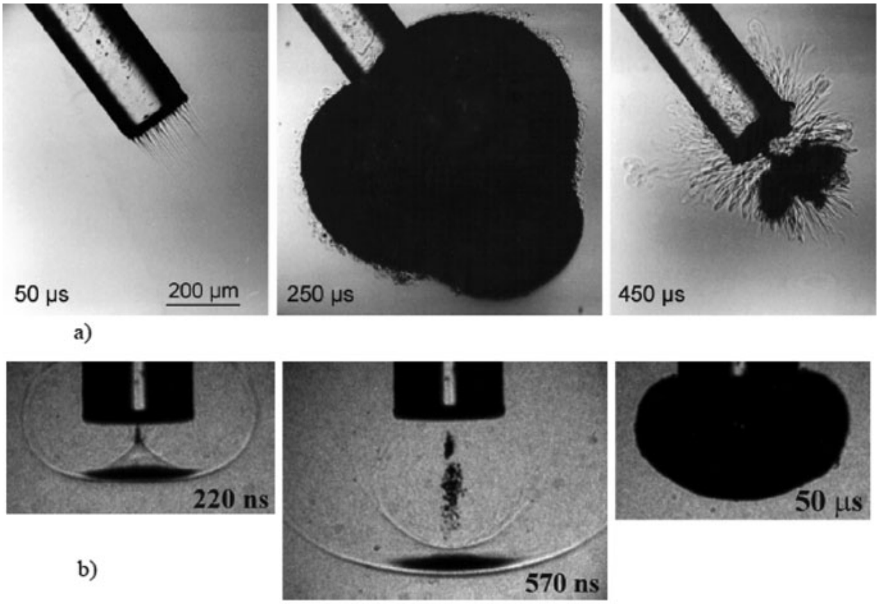

Fig. 14.28 Bubble formation in water without and with stress confinement (**a**) Bubble produced by a thulium laser pulse ($\lambda = 2.0\ \mu\text{m}$) of 500 mJ pulse energy and 300 µs duration (FWHM) applied through a 200-µm diameter optical fiber. Thermal Schlieren at the fiber tip mark the optical penetration depth. Schlieren around the expanded and collapsed bubble indicate that the liquid next to the bubble remains hot for some time. (**b**) Bubble formation under stress confinement conditions [38]. 6-ns pulses of 490 nm wavelength were transmitted through a 200-µm optical fiber submerged in an aqueous solution of Orange G dye with an optical penetration depth of 11 µm. Tensile stress waves originating from the stress release ("diffraction") at the edges of the fiber produce cavitation bubbles at the fiber axis where they overlap. After ≈ 5 µs, a vapor bubble appears directly at the fiber surface that reaches its maximum size at 50 µs. (Reprinted with permission from [38])

of phase transitions. When the rate of energy deposition is low and heterogeneous vaporization nuclei are present, the phase transition is governed by normal boiling and starts once a temperature in excess of the equilibrium saturation temperature (100°C at atmospheric pressure) has been reached that is sufficient to overcome the surface tension of the vaporization nuclei (Fig. 14.8). Due to the large specific volume of water vapor, bubbles of considerable size are formed even when only a small fraction of the water within the optical penetration depth is vaporized. When the rate of energy deposition is high and the stress confinement condition is not fulfilled, a phase explosion occurs once the spinodal limit is reached [185, 187]. The separation of the metastable liquid into saturated vapor and saturated liquid corresponds again to a partial vaporization. The fraction vaporized is below 50% and depends on the volumetric energy density as described by the theory of metastable liquids [45, 194, 195] (Section 14.4.4). For intermediate rates of energy deposition in the presence of heterogeneous nuclei, the phase transition occurs as explosive boiling. At very large radiant exposures and nanosecond pulse durations, supercritical conditions are produced and the heated volume is completely transformed to vapor as it expands to pressures below the critical point (Section 14.4.6).

With stress confinement, a thermoelastic stress wave is launched within a liquid volume directly adjacent to the fiber tip, and tensile stress waves are created due to the finite spatial extent of the absorbing liquid volume (Section 14.3). The tensile stress distribution can be described as a consequence of diffraction of the thermoelastic stress wave at the circular boundary of the acoustic source in front of the fiber tip. The ratio of the optical penetration depth ($1/\mu_a$) of the laser radiation to the diameter d of the fiber tip determines whether the cavitation-induced bubble formation occurs inside or outside the volume of energy deposition, which is the case for $\mu_a d \approx 1$, and $\mu_a \mathrm{d} << 1$, respectively [38, 196]. An example of cavitation-induced bubble formation outside the volume of energy deposition is shown in Fig. 14.28b. Using nanosecond pulses delivered though a 400 μm fiber into a medium with an optical penetration depth of 380 μm, cavitation could be created by a temperature rise as small as 33°C [195]. Similar absorption and stress confinement conditions are achieved with a Q-switched holmium laser in aqueous (water or blood) environments. A certain degree of stress confinement is also present during the individual intensity spikes of free-running holmium laser pulses. The tensile portion of the thermoelastic stress transients produced by these spikes leads to a transient lowering of the boiling temperature and to bubble formation from heterogeneous nuclei at temperatures well below 100°C [187].

The dynamics of bubble formation and growth depends on the number density and size of heterogeneous nuclei as well as on the specific path taken in the phase diagram. Therefore, no general temperature-threshold for bubble formation exists. The conditions leading to bubble formation must be determined in each individual case by establishing the dynamics of temperature and pressure produced by the laser irradiation.

The expansion of the hot ablation products is always inhibited in a liquid environment, and is confined further in cases where the fiber tip is placed in direct contact with the tissue surface. Thus for a given radiant exposure, higher temperatures and pressures can build up within the target as compared to ablation in a gaseous environment. Due to the higher pressures, liquid environments offer a more effective transduction of the laser energy into mechanical energy [197, 198]. As a result, the potential for mechanical collateral damage is much larger for ablation in liquid environments as compared to air [197, 199–206].

The expansion of the heated liquid volume produces a compressive stress transient followed by bubble formation. When the laser-induced stress transient possesses a sufficiently short rise time, its propagation results in the formation of a shock wave [206]. The large pressure in the laser-induced vapor bubble leads to a very rapid expansion that overshoots the equilibrium state where the internal bubble pressure equals the hydrostatic pressure. The increasing difference between the hydrostatic pressure and the falling internal bubble pressure then decelerates the expansion and brings it to a halt. At this point, the kinetic energy of the liquid during bubble expansion has been transformed into the potential energy of the expanded bubble. The bubble energy E_B [J] is related to the radius of the bubble at its maximum expansion, $R_{\max}$, and the difference between the hydrostatic pressure p_0 [Pa] and the vapor pressure p_v [Pa] inside the bubble by [207]

$$E_B = \frac{4\pi}{3}\,(p_0 - p_{\mathrm{v}})R_{\max}^3 \tag{14.18}$$

The expanded bubble collapses again due to the static background fluid pressure. The collapse compresses the bubble content into a very small volume, thus generating a very high pressure that can exceed 1 GPa for an approximately spherical bubble collapse [208]. The rebound of the compressed bubble interior leads again to the emission of a strong pressure transient into the surrounding liquid that can evolve into a shock wave [203, 204].

While the events during bubble generation are influenced strongly by the laser parameters, the subsequent bubble dynamics are influenced primarily by the properties of the fluid and the boundary conditions in the neighborhood of the laser focus. A spherical bubble produced in an unconfined liquid retains its spherical shape while oscillating, and the bubble collapse takes place at the site of bubble formation. However, when the bubble is formed near a material boundary, the collapse is asymmetric and associated with the formation of high-speed water jets that concentrate the bubble energy at some distance from the locus of bubble generation [201, 208]. When the bubble collapses in the vicinity of a rigid boundary, the jet is directed towards this boundary. The bubble collapse near an elastic, tissue-like boundary is characterized by the formation of two liquid jets that are directed both away from and towards the boundary and reach velocities as high as 960 m/s [208]. Jet formation is also induced by the fiber tip itself whereby the jet is usually directed away from the tip in the direction of the fiber axis [188, 209]. The jets have been shown to be responsible for collateral damage [209] and to increase the material removal [201, 202, 210].

The fraction of laser energy converted into the mechanical energy of the cavitation bubble depends on the laser pulse duration [191, 211]. Bubbles produced by free-running laser pulses with durations of several hundred microseconds expand during the laser pulse, and vaporization and condensation occur simultaneously in different bubble regions. Material is ablated at the bubble wall opposite to the fiber tip while vapor condenses in those regions of the bubble that are not exposed to the laser radiation [191, 211]. The bubble formation during the laser pulse limits the maximum energy density in the ablated target. The energy flow and condensation within the bubble further limits the maximum bubble size. By contrast, when nanosecond pulses are used for ablation, the bubble formation starts only towards the end of the laser irradiation [186, 187]. This corresponds to extremely high volumetric energy densities and temperatures adjacent to the fiber tip at radiant exposures well above the ablation threshold. As a result, the cavitation bubble expands to a much larger size than that produced by a free-running pulse with equal energy. Thus, cavitation can lead to structural deformation of the tissue adjacent to the ablation site that is much more pronounced than the direct ablative effect. These mechanical effects are sometimes desired because they enhance the cutting speed in liquid environments. However, the mechanical damage often compromises the high precision of the original ablation effect.

Cavitation-induced tissue deformation has had dramatic consequences in laser angioplasty [182]. The bubble dynamics produced ruptures within the vessel wall that often initiated an overactive healing response leading to restenosis [199]. Placement of an optical fiber tip in contact with the tissue further enhances the level of inertial confinement and can result in violent material ejection and tissue dissection [212–214]. Furthermore, the confinement of the ablation products by the ablation channel leads to an increase of collateral thermal damage because the heat within the ablation products is conducted back into the residual tissue [213, 215, 216].

Thermomechanical tissue injury can be significantly reduced when a tailored series of short pulses is delivered to the target rather than single pulses [1, 189, 190, 192]. When the pulse duration is sufficiently short to provide both stress and thermal confinement, the lowering of the ablation enthalpy in the stress confinement regime reduces the residual heat in the tissue [192, 211]. A reduction of cavitation effects is achieved by applying a pre-pulse with small energy followed by one or several ablation pulses with larger energy that are separated by time intervals of 50–100 μs. The pre-pulse produces a small cavitation bubble that is then filled by the ablation

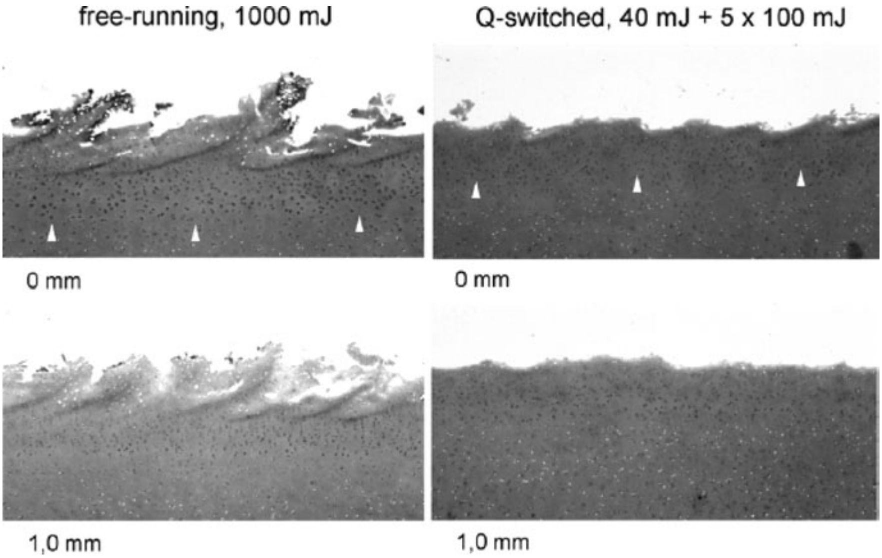

Fig. 14.29 Histological sections through ablated areas of cartilage that was irradiated with free-running thulium laser pulses (1000 mJ), and bursts of multiply Q-switched thulium-pulses (40 mJ + 5×100 mJ). The fiber was displaced by 0.4 mm between subsequent pulses. The distance between fiber tip and tissue surface was 0 mm (*top row*), and 1.0 mm (*bottom row*). The thermal damage zone (*arrows*) is much larger after free-running pulses, and the damage is more severe. Moreover, bursts of Q-switched pulses create smoother ablation crater walls than free-running pulses. Original magnification 20×

products produced by the subsequent pulses of higher energy. In this manner, no additional cavitation effects are produced, and tissue tearing and other mechanical side effects are minimized [189–192]. Moreover, the transient cavity created by the pre-pulse between fiber tip and tissue surface improves the optical transmission to the target which results in an increase of the ablation efficiency. The refinement of the tissue effects achieved by this technique is shown in Fig.14.29.

14.10 Control of Ablated Mass and Thermal and Mechanical Side Effects

In this section, we utilize predictions of ablation models as well as the qualitative insights formed in the previous sections to draw conclusions with regard to the control of ablated mass and thermal and mechanical side effects.

The heuristic ablation models described in Section 14.6.2 predict that, if the *removal of large amounts of material* is desired, the use of long laser pulses that achieve a steady-state-like ablation process will be more suitable than ablation based on a blow-off process. This arises because the ablated mass scales linearly with radiant exposure in a steady state ablation processes but logarithmically in a blow-off process (Eqs. (14.12) and (14.13)). However, the difference between the two types of ablation process becomes less pronounced if optical shielding by the ablation products is significant. A steady state process is most advantageous under conditions where the absorption of the incident laser beam by the ablation plume is markedly smaller than the absorption in the target tissue present in the blow-off situation. Very high ablation rates have been achieved using IR laser pulses with millisecond duration and used successfully for transmyocardial laser revascularization (TMR) where a deep hole is drilled across the full thickness of the myocardium during one fraction of the systolic cycle [214, 217].

When use of short laser pulses is required to minimize thermal side effects, the largest ablation efficiencies are achieved when the pulse duration is sufficiently short to guarantee not only thermal confinement but also stress confinement [67]. Stress confinement or inertial confinement conditions generally serve to lower the ablation threshold and increase the ablation efficiency (Section 14.4.7).

The most direct strategy to *control thermal side effects* involves the selection of a pulse duration that is sufficiently short to minimize heat diffusion during the laser pulse from the volume of energy deposition into the nonablated tissue (Eq. (14.3)). However, similar results may also be obtained using longer pulses if the velocity of the ablation front during the laser pulse is comparable or faster than the heat diffusion into the residual tissue. A theoretical analysis of this strategy was presented by Venugopalan and co-workers [43], and experimental evidence for its validity was presented by various authors [43, 142, 143, 218–220].

Thermal side effects can be diminished further by selecting laser pulse durations sufficiently short to provide both stress and thermal confinement because the lowering of the ablation enthalpy in the stress confinement regime reduces the residual heat in the tissue [192, 211]. This is shown in Fig. 14.29 where the thermal damage produced by ablation using free-running thulium laser pulses is compared to the damage zone produced by ablation using Q-switched thulium laser pulses. The first irradiation modality provides merely thermal confinement while the second modality provides both stress and thermal confinement.

When delivering multiple pulses to a single location, both the spatial extent and degree of the thermal injury are influenced by heat accumulation. The pulse repetition rate must be sufficiently low to avoid progressive accumulation of the residual heat within the tissue [143, 221]. An alternative strategy to avoid heat accumulation is to scan the laser beam in order to lengthen the time interval between subsequent exposures at each location within the ablated area.

In other instances, the heat accumulation occurring when series of laser pulses are applied can be used intentionally to create a coagulation effect in conjunction with precise laser ablation. Since precise tissue ablation requires both a small optical penetration depth and a short pulse duration, hemostasis is often not produced at the tissue surface. Hemostasis can be achieved by applying a series of pulses at radiant exposures just below the ablation threshold at sufficiently high repetition rate [222].

Mechanical side effects: In principle, high precision can be achieved by selecting a laser wavelength featuring a very small optical penetration depth combined with a short pulse duration sufficient to provide thermal confinement, and, if possible, also stress confinement. However, the production of extensive recoil stresses should be avoided to maintain the precision provided by a small optical penetration depth combined with thermal confinement. Extensive recoil stresses may degrade the smoothness of the ablated surface and/or induce collateral mechanical damage; especially in friable tissues. This restriction imposes an upper limit for the incident radiant exposure and implies that the finest tissue effects can be achieved by working close to the ablation threshold.

The confinement provided by a liquid environment increases the risk of mechanical side effects compared to ablation in air. Strategies to minimize these effects have been discussed in Section 14.8. On the other hand, for dissection procedures where precision and smoothness of the cut is less important than cutting efficiency and speed, the generation of disruptive effects is advantageous. In these cases, the highest ablation efficiency for a given average laser power can be achieved using a series of short pulses with high peak power and radiant exposures well above the ablation threshold.

14.11 Outlook and Challenges

During the past years, a framework has been created to identify relevant mechanisms governing pulsed laser tissue ablation techniques and to facilitate a rational formulation of irradiation strategies for specific tasks. Nevertheless, much work remains to further improve the understanding of pulsed laser ablation processes. While the detailed experimental study of the kinetics of tissue ablation combined with a careful consideration of the thermodynamics of phase transitions has provided a fairly complete qualitative understanding, predictive quantitative models are still absent to support it. Most current mechanistic models are limited to simple phase transitions such as surface vaporization and boiling. The challenge is to devise models that link material removal with both the complex phase change processes driving ablation (surface vaporization, phase explosion, vapor explosion, photodissociation, confined boiling etc.) as well as the dynamic tissue optical and mechanical properties that modulate the temperatures and pressures generated within the tissue prior to fracture. Moreover, once material removal is initiated, such models must consider that the recoil forces associated with ablation and the flow of the plume can both influence material removal.

Obviously, all these demands cannot be met by a simple comprehensive analytical model, and researchers must resort to computational approaches to fulfill these requirements. However, much information on dynamic material properties required for a faithful modeling is still missing. These data include dynamic optical properties (absorption and scattering coefficients), thermal properties (heat capacity, Grüneisen coefficient), and mechanical properties (elastic and shear modulus, ultimate tensile strength) that may depend on the magnitude and kinetics of the temperature, pressure, and strain rates achieved during the ablation process. This lack of data is now recognized to be even more important than was thought just a few years ago as recent experimental studies demonstrate that the temperatures and pressures involved in most ablation processes are more extreme than assumed previously [27]. Vogel and Venugopalan [1] provided a summary of the results of many of those studies, e.g. on surface temperature during ablation. We now know that pulsed laser tissue ablation is regularly associated with a temperature rise of hundreds to thousands K, recoil pressures of several hundred MPa, and strain rates on the order of 10^5–10^7 s^{-1}. Several of the above mentioned dynamic material properties are presently known only at the lower margin of this parameter space.

Molecular dynamics (MD) simulations are a powerful approach to gain insight into the pulsed laser ablation dynamics on a microscopic level with sub-nanosecond time resolution. However, to span the spatial and temporal scales usually encountered in realistic applications of tissue ablation, computational facilities are required that are currently still unavailable. To make such computations more tractable, MD simulations of laser ablation typically do not model the system on an atomic level but instead adopt a "breathing sphere" model where groups of atoms are treated as units [161, 164]. This simplification provides a realistic rate of vibrational relaxation of excited molecules, but only allows for an approximate treatment of photochemical reactions. However, it has enabled the calculation of the sequence of events initiated by instantaneous energy deposition on temporal and spatial scales as large as 2 ns and 1 μm, respectively, while maintaining high temporal (<5 ps) and spatial (<5 nm) resolution [166]. To simulate the more common case of laser energy deposition during the ablation process and incorporate plume dynamics, shielding, and recoil-induced material ejection, the MD simulations must be combined with continuum mechanical approaches or/and Monte Carlo simulations on a mesoscopic level.

The first steps in this direction have been already made [164] but there is still a long way to go to establish numerical tools that can treat ablation dynamics on microscopic, mesoscopic and macroscopic level and link the results to experimentally observable parameters.

References

1. Vogel A and Venugopalan V. Mechanisms of pulsed laser ablation of biological tissues. *Chem. Rev.*, 103:577–644 (2003).
2. Vogel A, Noack J, Hüttman, G, and Paltauf, G. Mechanisms of femtosecond laser nanosurgery of cells and tissues. *Appl. Phys. B*, 81:1015–1047 (2005).
3. Silver FH. *Biological materials: Structure, mechanical properties, and modeling of soft tissue*. New York University, New York and London, 229 pp (1987).
4. Nimni ME and Harkness RD. Molecular structure and functions of collagen. In: ME Nimni (ed) *Collagen. Vol. I Biochemistry*. CRC, Boca Raton, pp. 1–77 (1988).
5. Linsenmayer TF. Collagen. In: ED Hay (ed) *Cell biology of extracellular matrix*. Plenum, New York and London, , 2nd edition, pp. 7–44 (1991).
6. Vaezy S and, Clark JI. A quantitative analysis of transparence in the human sclera and cornea using Fourier methods. *J. Microsc.*, 163:85–94 (1991).
7. Nomura S, Hiltner A, Lando JB, and Baer E. Interaction of water with native collagen. *Biopolymers*, 16:231–246 (1977).
8. Cheong W-F. Summary of optical properties. In: AJ Welch, MJC van Gemert (eds) *Optical-thermal response of laser-irradiated tissue*. Plenum, New York, pp. 275–304 (1995).
9. Carp A, Prahl SA, and Venugopalan V. Radiative transport in the delta-P_1 approximation: Accuracy of fluence rate and optical penetration depth predictions in turbid semi-infinite media. *J. Biomed. Opt.*, 9:632–647 (2004).
10. Vodopyanov KL. Saturation studies of H_2O and HDO near 3400 cm^{-1} using intense picosecond laser pulses. *J. Chem. Phys.*, 94:5389–5393 (1991).
11. Walsh JT and Cummings JP. Effect of the dynamic optical properties of water on midinfrared laser ablation. *Lasers Surg. Med.*, 15:295–305 (1994).
12. Shori R, Walston AA, Stafsudd OM, Fried D, and Walsh JT. Quantification and modeling of the dynamic changes in the absorption coefficient of water at 2.94 μm. *IEEE J. Sel. Top. Quant. Electron.*, 7:959–970 (2002).
13. Staveteig PT and Walsh JT. Dynamic 193-nm optical properties of water. *Appl. Opt.*, 35:3392–3403 (1996).
14. Yamada H. *Strength of biological materials*. Robert E. Krieger, Huntington, NY (1970).
15. Vogel HG. Influence of age, treatment with corticosteroids and strain rate on mechanical properties of rat skin. *Biochim. Biophys. Acta*, 286:79–83 (1972).
16. Haut RC. The effects of orientation and location on the strength of dorsal rat skin in high and low speed tensile failure experiments. *Trans. ASME Biomed. Eng.,* 111, 136–140 (1989).
17. Dombi GW, Haut RC, and Sullivan WG. Correlation of high-speed tensile strength with collagen content in control and lathyritic rat skin. *J. Surg. Res.*, 54: 21–28 (1993).
18. Stryer L. *Biochemistry*. WH Freeman and Company, San Francisco (1987).
19. Thomsen S. Pathological analysis of photothermal and photomechanical effects of laser-tissue interactions. *Photochem. Photobiol.*, 53:825–835 (1991).
20. Allain JC, Le Lous M, Cohen-Solal L, Bazin S, and Maroteaux P. Isometric tensions developed during the hydrothermal swelling of rat skin. *Connect. Tissue Res.*, 7:127–133 (1980).
21. Kampmeier J, Radt B, Birngruber R, and Brinkmann R. Thermal and biomechanical parameters of porcine cornea. *Cornea*, 19:355–363 (2000).
22. Asiyo-Vogel MN, Brinkmann R, Notbohm H, Eggers R, Lubatschowski H, Laqua H, and Vogel A. Histologic analysis of thermal effects of laser thermokeratoplasty and corneal

ablation using Sirius-red polarization microscopy. *J. Cataract Refract. Surg.*, 23:515–526 (1997).

23. Le Lous M, Flandin F, Herbage D, and Allain JC. Influence of collagen denaturation on the chemorheological properties of skin, assessed by differential scanning calorimentry and hydrothermal isometric tension measurement. *Biochim. Biophys. Acta*, 717:295–300 (1982).
24. Henriques FC. Studies of thermal injury. V. The predictability and the significance of thermally induced rate processes leading to irreversible epidermal injury. *Arch. Pathol.*, 43, 489–502 (1947).
25. Simankowskii .M, Mackanos MA, Irani AR, O'Connel-Rodwell CE, Contag CH, Schwettman HA, and Palanker DV. Cellular tolerance to pulsed hyperthermia. *Phys. Rev. E*, 74:011915, 1–7 (2006).
26. Harris DM, Fried D, Reinisch L, Bell T, Schlachter D, From L, and Burkart J. Eyelid resurfacing. *Lasers Surg. Med.*, 25:107–122 (1999).
27. Apitz I and Vogel A. Material ejection in nanosecond Er:YAG laser ablation of water, liver, and skin. *Appl. Phys. A*, 81:329–228 (2005).
28. Carslaw HS and Jaeger JC. *Conduction of heat in solids.* Oxford University, Oxford, 2nd edition (1959).
29. Anderson RR and Parrish JA. Selective photothermolysis – precise microsurgery by selective absorption of pulsed radiation. *Science*, 220:524–527 (1983).
30. Jacques S. Role of tissue optics and pulse duration on tissue effects during high-power laser irradiation. *Appl. Opt.*, 32:2447–2454 (1993).
31. Venugopalan V, Nishioka NS, and Mikic BB. The thermodynamic response of soft biological tissues to pulsed ultraviolet laser radiation. *Biophys. J.*, 69:1259–1271 (1995).
32. Venugopalan V, Nishioka NS, and Mikic BB. Thermodynamic response of soft biological tissues to pulsed infrared laser radiation. *Biophys. J.*, 70:2981–2933 (1996).
33. Paltauf G and Dyer PE. Photomechanical processes and effects in ablation. *Chem. Rev.*, 103:487–518 (2003).
34. Sigrist MW. Laser generation of sound waves in liquids and gases. *J. Appl. Phys.*, 60:R83–R121 (1986).
35. Bushnell JC and McCloskey DJ. Thermoelastic stress generation in solids. *J. Appl. Phys.*, 39:5541–5546 (1968).
36. Itzkan I, Albagli D, Dark ML, Perelman LT, von Rosenberg C, and Feld M. The thermoelastic basis of short pulsed laser ablation of biological tissue. *Proc. Natl. Acad. Sci. USA*, 92:1960–1964 (1995).
37. Paltauf G and Schmidt-Kloiber H. Microcavity dynamics during laser-induced spallation of liquids and gels. *Appl. Phys. A*, 62:303–311 (1996).
38. Frenz M, Paltauf, G, and Schmidt-Kloiber H. Laser-generated cavitation in absorbing liquid induced by acoustic diffraction. *Phys. Rev. Lett.*, 76:3546–3549 (1996).
39. Paltauf G and Schmidt-Kloiber H. Photoacoustic cavitation in spherical and cylindrical absorbers. *Appl. Phys. A*, 68:525–531 (1999).
40. Miotello A and Kelly R. Critical assessment of thermal models for laser sputtering at high fluences. *Appl. Phys. Lett.*, 67:3535–3537 (1995).
41. Schrage RW. *A theoretical study of interphase mass transfer*. Columbia University, New York (1953).
42. Yablon AD, Nishioka NS, Mikić, BB, and Venugopalan V. Physical mechanisms of pulsed infrared laser ablation of biological tissues. *Proc. SPIE*, 3343:69–77 (1998).
43. Venugopalan V, Nishioka NS, and Mikic BB. The effect of laser parameters on the zone of thermal injury produced by laser ablation of biological tissue. *Trans. ASME J. Biomech. Eng.*, 116:62–70 (1994).
44. Miotello A and Kelly R. Laser-induced phase explosion: New physical problems when a condensed phase approaches the thermodynamic critical temperature. *Appl. Phys. A*, 69:S67–S73 (1999).
45. Debenedetti P. *Metastable liquids: Concepts and principles.* Princeton University, Princeton, NJ (1996).
46. Skripov VP. *Metastable liquids.* Wiley, New York (1974).

47. Skripov VP, Sinitsyn, EN, Pavlov, PA, Ermakov, GV, Muratov, GN, Bulanov, NV, and Baidakov G. *Thermophysical properties of liquids in the metastable (superheated) state*. Gordon and Breach Science, New York (1988).
48. Apfel RE. Water superheated to 279.5°C at atmospheric pressure. *Nature Phys. Sci.*, 238:63–64 (1972).
49. Martynyuk MM. Vaporization and boiling of liquid metal in an exploding wire. *Sov. Phys. Tech. Phys.*, 19:793–797 (1974).
50. Martynyuk MM. Phase explosion of a metastable fluid. *Combust. Explos. Shock Waves*, 13:178–191 (1977).
51. Frenkel II. *Kinetic theory of liquids.* Dover, New York (1955).
52. Kiselev SB. Kinetic boundary of metastable states in superheated and stretched liquids. *Physica A*, 269:252–268 (1999).
53. Majaron B, Plestenjak P, and Lukac M. Thermo-mechanical laser ablation of soft biological tissue: Modelling the micro-explosions. *Appl. Phys. B*, 69:71–80 (1999).
54. Verdaasdonk RM, Borst C, and van Germert MJC. Explosive onset of continuous wave laser tissue ablation. *Phys. Med. Biol.*, 35:1129–1144 (1990).
55. LeCarpentier GL, Motamedi M, McMath LP, Rastegar S, and Welch AJ. Continuous wave laser ablation of tissue: Analysis of thermal and mechanical events. *IEEE Trans. Biomed. Eng.*, 40:188–200 (1993).
56. Frenz M, Romano V, Zweig AD, Weber HP, Chapliev NI, and Silenok AV. Instabilities in laser cutting of soft media. *J. Appl. Phys.*, 66:4496–4503 (1989).
57. Zweig AD. A thermo-mechanical model for laser ablation. *J. Appl. Phys.*, 70:1684–1691 (1991).
58. Lu Q. Thermodynamic evolution of phase explosion during high-power nanosecond laser ablation. *Phys. Rev. E*, 67:016410 (5 pages) (2003).
59. Dingus RS and Scammon RJ. Grüneisen-stress induced ablation of biological tissue. *Proc. SPIE*, 1427:45–54 (1991).
60. Dingus RS, Curran DR, Oraevsky AA, and Jacques SL. Microscopic spallation process and its potential role in laser-tissue ablation. *Proc. SPIE*, 2134A:434–445 (1994).
61. Paltauf G and Schmidt-Kloiber H. Model study to investigate the contribution of spallation to pulsed laser ablation of tissue. *Lasers Surg. Med.*, 16:277–287 (1995).
62. Oraevsky AA, Jacques SL, Esenaliev RO, and Tittel FK. Pulsed laser ablation of soft tissue, gels, and aqueous solutions at temperatures below 100°C. *Lasers Surg. Med.*, 18:231–240 (1996).
63. Duvall GE and Fowles GR. Shock waves. In: RS Bradley (ed) *High pressure physics and chemistry.* Academic, New York, pp. 209–291 (1963).
64. Zel'dovich YB and Raizer YP. *Physics of shock waves and high temperature hydrodynamic phenomena*, Vol. I and II. Academic, New York and London (1966).
65. Lu Q, Mao SS, Mao X, and Russo RE. Delayed phase explosion during high-power nanosecond laser ablation of silicon. *Appl. Phys. Lett.*, 80:3072–3074 (2002).
66. Vogel A and Noack J. Shock wave energy and acoustic energy dissipation after laser-induced breakdown. *Proc. SPIE*, 3254:180–189 (1998).
67. Albagli D, Perelman LT, Janes GS, von Rosenberg C, Itzkan I, and Feld M. Inertially confined ablation of biological tissue. *Lasers Life Sci.*, 6:55–68 (1994).
68. Kawamura Y, Toyoda K, and Namba S. Effective deep ultraviolet photoetching of polymethyl methacrylate by an excimer laser. *Appl. Phys. Lett.*, 40:374–375 (1982).
69. Srinivasan R and Mayne-Barton V. Self-developing photoetching of poly(ethylene terephthalate) films by far-ultraviolt excimer laser radiation. *Appl. Phys. Lett.*, 41:576–578 (1982).
70. Trokel SL, Srinivasan R, and Braren B. Excimer laser surgery of the cornea. *Am J. Ophthalmol.*, 96:710–715 (1983).
71. Srinivasan R and Leigh W. Ablative photodecomposition. Action of far-ultraviolet (193 nm) laser radiation on poly(ethylene terephthalate) films. *Am. J. Chem. Soc.*, 104:6784–6785 (1982).

72. Srinivasan R. Ablation of polymers and biological tissues using ultraviolet lasers. *Science*, 234:559–565 (1986).
73. Jellinek HHG and Srinivasan R. Theory of etching polymers by far-ultraviolet, high-intensity pulsed laser and long-term radiation. *J. Phys. Chem.*, 88:3048–3051 (1984).
74. Palmer BJ, Keyes T, Clarke RH, and Isner JM. Theoretical study of ablative photodecomposition in polymeric solids. *J. Phys. Chem.*, 93:7509–7516 (1989).
75. Garrison BJ and Srinivasan R. Laser ablation of organic polymers: Microscopic models for photochemical and thermal processes. *J. Appl. Phys.*, 57:2909–2914 (1985).
76. Srinivasan R and Braren B. Ultraviolet ablation of organic polymers. *Chem. Rev.*, 89:1303–1316 (1989).
77. Yeh C. Laser ablation of polymers. *J. Vac. Sci. Technol.*, A4:653–658 (1986).
78. Isner JM and Clarke RH. The paradox of thermal ablation without thermal injury. *Lasers Med. Sci.*, 2:165–173 (1987).
79. Wayne CE and Wayne RP. *Photochemistry.* Oxford University, Oxford (1996).
80. Ashfold MNR and Cook PA. Photochemistry with VUV photons. In:RA Meyers (ed) *Encyclopedia of physical science and technology*. Academic, 3rd edition (2002).
81. Davis GM, Gower MC, Fotakis C. Efthimiopoulos T, and Argyrakis P. Spectroscopic studies of ArF laser photoablation of PMMA. *Appl. Phys. A*, 36:27–30 (1985).
82. Dyer PE and Sidhu J. Excimer laser ablation and thermal coupling efficiency to polymer films. *J. Appl. Phys.*, 57:1420–1422 (1985).
83. Gorodetsky G, Kazyaka T G, Melcher RL, and Srinivasan R. Calorimetric and acoustic study of ultraviolet laser ablation of polymers. *Appl. Phys. Lett.*, 46:828–830 (1985).
84. Brunco DP, Thompson MO, Otis CE, and Goodwin PM. Temperature measurements of polyimide during KrF excimer laser ablation. *J. Appl. Phys.*, 72:4344–4350 (1992).
85. Otis CE, Braren B, Thompson MO, Brunco D, and Goodwin PM. Mechanisms of excimer laser ablation of strongly absorbing systems. *Proc. SPIE*, 1856:132–142 (1993).
86. Sutcliffe E and Srinivasan R. Dynamics of UV laser ablation of organic polymer surfaces. *J. Appl. Phys.*, 60:3315–3322 (1986).
87. Srinivasan R. Ablation of polyimide (Kapton$^{\mathrm{TM}}$) films by pulsed (ns) ultraviolet and infrared (9.17 µm) laser. *Appl. Phys. A*, 56:417–423 (1993).
88. Lippert T and Dickinson JT. Chemical and spectroscopic aspects of polymer ablation: Special features and novel directions. *Chem. Rev.*, 103:453–485 (2003).
89. Pettit GH. The physics of ultraviolet laser ablation. In: RW Waynant (ed) *Lasers in medicine*. CRC, Boca Raton, pp. 109–133 (2002).
90. Andrew JE, Dyer PE, Forster D, and Key PH. Direct etching of polymeric materials using a XeCl laser. *Appl. Phys. Lett.*, 43:717–719 (1983).
91. Küper S, Madaressi S, and Stuke M. Photofragmentation pathways of a PMMA model compound under UV excimer laser ablation conditions. *J. Phys. Chem.*, 94:7514–7518 (1990).
92. Kitai MS, Popkov, VL, Semchishen VA, and Kharizov AA. The physics of UV laser cornea ablation. *IEEE J. Quant. Electron.*, 27:302–307 (1991).
93. Arnold N and Bityurin N. Model for laser-induced thermal degradation and ablation of polymers. *Appl. Phys. A*, 68:615–625 (1999).
94. Nikogosyan DN and Görner H. Laser-induced photodecomposition of amino-acids and peptides: Extrapolation to corneal collagen. *IEEE J. Sel. Top. Quant. Electron.*, 5:1107–1115 (1999).
95. Bityurin N, Luk'yanchuk BS, Hong MH, and Chong TC. Models for laser ablation of polymers. *Chem Rev.*, 103:519–552 (2003).
96. Schmidt H, Ihlemann J, Wolff-Rottke B, Luther K, and Troe J. Ultraviolet laser ablation of polymers: Spot size, pulse duration, and plume attenuation effects explained. *J. Appl. Phys.*, 83:5458–5468 (1998).
97. Yingling YG, Zhigilei LV, and Garrison BJ. The role of photochemical fragmentation in laser ablation: A molecular dynamics study. *J. Photochem. Photobiol.*, 145:173–181 (2001).

98. Oraevsky AA, Jacques SL, Pettit GH, Saidi IS, Tittel FK, and Henry PD. XeCl laser ablation of atherosclerotic aorta: Optical properties and energy pathways. *Lasers Surg. Med.*, 12:585–597 (1992).
99. Vogel A, Apitz I, Freidank S, and Dijkink R. Sensitive high-resolution white-light Schlieren technique with large dynamic range for the investigation of ablation dynamics. *Opt. Lett.*, 31:1812–1814 (2006).
100. Hecht E and Zajac A. *Optics*. Addison Wesley, Reading, MA (1977).
101. Walsh JT and Deutsch TF. Measurement of Er:YAG laser ablation plume dynamics. *Appl. Phys. B*, 52:217–224 (1991).
102. Bor Z, Hopp B, Rácz B, Szabó G, Ratkay I, Süveges I, Füst A, and Mohay J. Plume emission, shock wave and surface wave formation during excimer laser ablation of the cornea. *Refract. Corneal Surg. (Suppl.)*, 9: S111–S115 (1993).
103. Cummings JP and Walsh JT. Q-switched ablation of tissue: Plume dynamics and the effect of tissue mechanical properties. *Proc. SPIE*, 1646:242–253 (1992).
104. Krueger RR and Trokel SL. Quantitation of corneal ablation by ultraviolet laser light. *Arch. Ophthalmol.*, 103:1741–1742 (1985).
105. Noack J, Tönnies R, Hohla C, Birngruber R, and Vogel A. Influence of ablation plume dynamics on the formation of central islands in excimer laser photorefractive keratectomy. *Ophthalmology*, 104:823–830 (1997).
106. Arnold N, Gruber J, and Heitz J. Spherical expansion of the vapor plume into ambient gas: An analytical model. *Appl. Phys. A*, 69:S87–S93 (1999).
107. Brode HL. Blast wave from a spherical charge. *Phys. Fluids*, 2:217–229 (1959).
108. Taylor G. The formation of a blast wave by a very intense explosion. I Theoretical discussion. *Proc. Roy. Soc. A*, 201:159–186 (1950).
109. Sedov LI. *Similarity and dimensional methods in mechanics*. Academic, New York (1959).
110. Landau LD and Lifschitz EM. *Fluid mechanics*. Pergamon, Oxford, 2nd edition (1987).
111. Sakurai A. On the propagation and structure of a blast wave, I. *J. Phys. Soc. Japan*, 8:662–671 (1953).
112. Sakurai A. On the propagation and structure of a blast wave, II. *J. Phys. Soc. Japan*, 9:256–266 (1954).
113. Freiwald DA and Axford RA. Approximate spherical blast theory including source mass. *J. Appl. Phys.*, 46:1171–1174 (1975).
114. Kelly R and Braren B. On the direct observation of the gas dynamics of laser-pulse sputtering of polymers. Part I: Analytical considerations. *Appl. Phys. B*, 53:160–169 (1991).
115. Kelly R and Miotello A. Pulsed-laser sputtering of atoms and molecules. Part I: Basic solutions for gas-dynamic effects. *Appl. Phys. B*, 57:145–158 (1993).
116. Dyer PE and Sidhu J. Spectroscopic and fast photographic studies of excimer laser polymer ablation. *J. Appl. Phys.*, 64:4657–4663 (1988).
117. Jones DL. Intermediate strength blast wave. *Phys. Fluids*, 11:1664–1667 (1968).
118. Stauter C, Gérard P, Fontaine J, and Engel T. Laser ablation acoustical monitoring. *Appl. Surf. Sci.*, 109/110:174–178 (1997).
119. Freiwald DA. Approximate blast wave theory and experimental data for shock trajectories in linear explosive-driven shock tubes. *J. Appl. Phys.*, 43:2224–2226 (1972).
120. Chen Z, Bogaerts A, and Vertes A. Phase explosion in atmospheric pressure infrared laser balation from water-rich targets. *Appl. Phys. Lett.*, 89:041503 (2006).
121. Nahen K and Vogel A. Shielding by the ablation plume during Er:YAG Laser ablation. *J. Biomed. Opt.*, 7:165–178 (2002).
122. Nahen K and Vogel A. Investigations on acoustic on-line monitoring of IR laser ablation of burned skin. *Lasers Surg. Med.*, 25:69–78 (1999).
123. Nahen K and Vogel A. Acoustic signal characteristics during IR laser ablation, and their consequences for acoustic tissue discrimination. *Proc. SPIE*, 3914:166–176 (2000).
124. Vogel A, Kersten B, and Apitz I. Material ejection in free-running Er:YAG laser ablation of water, liver and skin by phase explosion, confined boiling, recoil-induced expulsion and flow-induced suction. *Proc. SPIE*, 4961:40–47: (2003).

125. Hibst R. *Technik, Wirkungsweise und medizinische Anwendungen von Holmium- und Erbium-Lasern*. Ecomed, Landsberg, pp. 1–120 (in German) (1996).
126. Puliafito CA, Stern D, Krueger RR, and Mandel ER. High-speed photography of excimer laser ablation of the cornea. *Arch. Ophthalmol.*, 105:1255–1259 (1987).
127. Bäuerle D. *Laser processing and chemistry.* Springer, Berlin (2000).
128. Cummings JP and Walsh JT. Tissue tearing caused by pulsed laser-induced ablation pressure. *Appl. Opt.*, 32:494–503 (1993).
129. Phipps CR, Harrison RF, Shimada T, York GW, Turner TP, Corlis XF, Steele HS, Haynes LC, and King TR. Enhanced vacuum laser-impulse coupling by volume absorption at infrared wavelengths. *Lasers Particle Beams*, 8:281–297 (1990).
130. Dyer PE and Al-Dhahir RK. Transient photoacoustic studies of laser tissue ablation. *Proc. SPIE*, 1202:46–60 (1990).
131. Könz F, Frenz M, Pratisto H, Weber HP, Lubatschowski H, Kermani O, Ertmer W, Altermatt HJ, and Schaffner T. Thermal and mechanical damage of corneal tissue after free-running and Q-switched mid-infrared laser ablation. *Proc. SPIE*, 2077:78–86 (1994).
132. Esenaliev RO, Oraevsky AA, Letokhov VS, Karabutov AA, and Malinsky TV. Studies of acoustical and shock waves in the pulsed laser ablation of biotissue. *Lasers Surg. Med.*, 13:470–484 (1993).
133. Engel OGJ. Crater depth in fluid impacts. *J. Appl. Phys.*, 37:1798–1808 (1966).
134. Prosperetti A and Oguz HN. The impact of drops on liquid surfaces and the underwater noise of rain. *Ann. Rev. Fluid Mech.*, 25:577–602 (1993).
135. Walsh JT and Deutsch TF. Er:YAG laser ablation of tissue: Measurement of ablation rates. *Lasers Surg. Med.*, 9:327–337 (1989).
136. Duck FA. *Physical properties of tissue*. Academic, London (1990).
137. Fung YC. *Biomechanics: Mechanical properties of living tissues.* Springer, New York (1993).
138. Watanabe S, Flotte TJ, McAucliffe DJ, and Jacques SL. Putative photoacoustic damage in skin induced by pulsed ArF excimer laser. *J. Invest. Dermatol.*, 90, 761–766 (1988).
139. Yashima Y, McAuclffe DJ, Jacques SL, and Flotte TJ. Laser-induced photoacoustic injury of skin: Effect of inertial confinement. *Lasers Surg. Med.*, 11:62–68 (1991).
140. Pini R, Rossi F, Salimbeni S, Siano S, Vannini M, Carones F, Trabucci G, Brancato R, and Gobbi PG. Experimental investigation on acoustic phenomena induced inside the eyeball by excimer laser ablation of the cornea. *Proc. SPIE*, 2632:25–29 (1996).
141. Nishioka NS and Domankevitz Y. Reflectance during pulsed holmium laser irradiation of tissue. *Lasers Surg. Med.*, 9:375–381 (1989).
142. Kaufmann R and Hibst R. Pulsed erbium:YAG laser ablation in cutaneous surgery. *Lasers Surg. Med.*, 19:324–330 (1996).
143. Venugopalan V, Nishioka NS, and Mikic BB. The effect of CO_2 laser pulse repetition rate on tissue ablation rate and thermal damage. *IEEE Trans Biomed. Eng.*, 38:1049–1052 (1991).
144. Walsh JT and Deutsch TF. Pulsed CO_2 laser tissue ablation: Measurement of the ablation rate. *Lasers Surg. Med.*, 8:264–275 (1988).
145. Shimmick JK, Telfair WB, Munnerlyn CR, Bartlett JD, and Trokel SL. Corneal ablation profilometry and steep central islands. *J. Refract. Surg.*, 13:235–245 (1997).
146. Zhigilei LV and Garrison BJ. Molecular dynamics simulation study of the fluence dependence of particle yield and plume composition in laser desorption and ablation of organic solids. *Appl. Phys. Lett.*, 74:1341–1343 (1999).
147. Yingling YG, Zhigilei LV, Garrison BJ, Koubenakis A, Labrakis J, and Georgiou S. Laser ablation of bicomponent systems: A probe of molecular ejection mechanisms. *Appl. Phys. Lett.*, 78:1631–1633 (2001).
148. Cross FW, Al-Dhahir RK, Dyer PE, and MacRobert AJ. Time-resolved photoacoustic studies of vascular tissue ablation at three laser wavelengths. *Appl. Phys. Lett.*, 50:1019–1021 (1987).

149. Domankevitz Y and Nishioka NS. Measurement of laser ablation threshold with a high-speed framing camera. *IEEE J. Quant. Electon.*, 26:2276–2278 (1990).
150. Walsh JT and Deutsch TF. Pulsed CO_2 laser ablation of tissue: Effect of mechanical properties. *IEEE Trans. Biomed. Eng.*, 36(12):1195–1201 (1989).
151. Deutsch TF and Geis MW. Self-developing UV photoresist using excimer laser exposure. *J. Appl. Phys.*, 54:7201–7204 (1983).
152. Puliafito CA, Wong K, and Steinert RF. Quantitative and ultrastructural studies of excimer laser ablation of the cornea at 193 and 248 nanometers. *Lasers Surg. Med.*, 7:155–159 (1987).
153. Pettit GH and Ediger MN. Corneal tissue absorption coefficients for 193- and 213-nm ultraviolet radiation. *Appl. Opt.*, 35:3386–3391 (1996).
154. Langerholc J. Moving phase-transitions in laser-irradiated biological tissue. *Appl. Opt.*, 18:2286–2293 (1979).
155. McKenzie AL. A three-zone model of soft-tissue damage by a CO_2 laser. *Phys. Med. Biol.*, 31:967–983 (1986).
156. McKenzie AL. An extension of the three-zone model to predict depth of tissue damage beneath Er:YAG and Ho:YAG laser excisions. *Phys. Med. Biol.*, 34:107–114 (1989).
157. Partovi F, Izatt JA, Cothren RM, Kittrell C, Thomas JE, Strikwerda S, Kramer JR, and Feld MS. A model for thermal ablation of biological tissue using laser radiation. *Lasers Surg. Med.*, 7:141–154 (1987).
158. Gerstmann, M, Sagi, A, Avidor-Zehavi, A, Katzir, A, and Akselrod, S. Model simulation of biological damage in tissue exposed to CO_2 laser irradiation. *Opt. Eng.*, 32:291–297 (1993).
159. Olmes A, Franke HG, Bänsch E, Lubatschowski H, Raible M, Dziuk G, and Ertmer W. Modeling of infrared soft-tissue photoablation process. *Appl. Phys. B*, 65:659–666 (1997).
160. Zweig AD and Weber HP. Mechanical and thermal parameters in pulsed laser cutting of tissue. *IEEE J. Quant. Electron.*, 23:1787–1793 (1987).
161. Zhigilei LV, Kodali PBS, and Garrison BJ. Molecular dynamics model for laser ablation and desorption of organic solids. *J. Phys. Chem. B*, 101:2028–2037 (1997).
162. Zhigilei LV, Kodali PBS, and Garrison BJ. A microscopic view of laser ablation. *J. Phys. Chem. B*, 102:2845–2853 (1998).
163. Zhigilei LV and Garrison BJ. Microscopic mechanisms of laser ablation of organic solids in the thermal and stress confinement irradiation regimes. *J. Appl. Phys.*, 88:1281–1298 (2000).
164. Zhigilei LV, Leveugle E, Garrison B, Yingling YG, and Zeifman MI. Computer simulations of laser ablation of molecular substrates. *Chem. Rev.*, 103:321–347 (2003).
165. Dou Y, Winograd N, Garrison B, and Zhigilei L. Substrate-assisted initiation od proteins embedded in water films. *J. Phys. Chem. B*, 107:2362–2365 (2003).
166. Knochenmuss R and Zhigilei LV. Molecular dynamics model of Ultraviolet matrix-assisted laser desorption/ionization including ionization process. *J. Phys. Chem. B*, 109:22947–22957 (2005).
167. Leveugle E and Zhigilei LV. Microscopic mechanisms of short pulse laser spallation of molecular solids. *Appl. Phys. A*, 79:753–756 (2004).
168. Leveugle E, Ivanov DS, and Zhigilei LV. Photomechanical spallation of molecular and metal targets: Molecular dynamics study. *Appl. Phys. A*, 79:1643–1655 (2004).
169. Krauss JM, Puliafito CA, and Steinert RF. Laser interactions with the cornea. *Surv. Ophthalmol.*, 31:37–53 (1986).
170. Puliafito CA, Steinert RF, Deutsch TF, Hillenkamp F, Dehm EJ, and Adler CM. Excimer laser ablation of the cornea and lens. *Ophthalmology*, 92:741–748 (1985).
171. Lane RJ, Linsker R, Wynne JJ, Torres A, and Geronemus RG. Ultraviolet-laser ablation of skin. *Arch. Dermatol.*, 121:609–617 (1985).
172. Seiler T, Marshall J, Rotherty S, and Wollensak J. The potential of an infrared hydrogen fluoride (HF) laser (3,0 μm) for corneal surgery. *Lasers Ophthalmol.*, 1:49–60 (1986).
173. Loertscher H, Mandelbaum S, Parrish RK III, and Parel JM. Preliminary report on corneal incisions created by a hydrogen fluoride laser. *Am. J. Ophthalmol.*, 102:217–221 (1986).

174. Bende T, Kriegerowski M, and Seiler T. Photoablation in different ocular tissues performed with an Erbium:YAG laser. *Lasers Light Ophthalmol.*, 2:263–269 (1989).
175. Wolbarsht ML. Laser surgery: CO_2 or HF. *IEEE J. Quant. Electron.*, 20:1427–1432 (1984).
176. Telfair WB, Bekker C, Hoffman HJ, Yoder PR Jr, Norquist RE, Eiferman RA, and Zenzie HH. Histological comparison of corneal ablation with Er:YAG laser, Nd:YAG optical parametric oscillator, and excimer laser. *J. Refract. Surg.*, 16:40–50 (2000).
177. Yablon AD, Nishioka NS, Mikic BB, and Venugopalan V. Measurement of tissue absorption coefficients by use of interferometric photothermal spectroscopy. *Appl. Opt.*, 38:1259–1272 (1999).
178. Srinivasan R, Dyer PE, and Braren B. Far-Ultraviolet laser ablation of the cornea: Photoacoustic studies. *Lasers Surg. Med.*, 6:514–519 (1987).
179. Ishihara M, Arai T, Sato S, Morimoto Y, Obara M, and Kikuchi M. Measurement of the surface temperature of the cornea during ArFexcimer laser ablation by thermal radiatiometry with a 15 nanosecond time response. *Lasers Surg. Med.*, 30:54–59 (2002).
180. Kermani O, Koort HJ, Roth E, and Dardenne MU. Mass-spectroscopic analysis of excimer laser ablated material from human corneal tissue. *J. Cataract Refract. Surg.*, 14:638–641 (1988).
181. Hahn DW, Ediger MN, and Petttit GH. Dynamics of ablation plume particles generated during excimer laser corneal ablation. *Lasers Surg. Med.*, 16:384–389 (1995).
182. Isner JM, deJesus S R, Clarke RH, Gal D, Rongione AJ, and Donaldson RF. Mechanism of laser ablation in an absorbing flow field. *Lasers Surg. Med.*, 8:543–554 (1988).
183. Deckelbaum LI. Coronary laser angioplasty. *Lasers Surg. Med.*, 14:101–110 (1994).
184. Köstli KP, Frenz M, Weber HP, Paltauf G, and Schmidt-Kloiber H. Optoacoustic measurements of water, bone and cartilage with an infrared-OPO. *Proc. SPIE*, 3601:310–318 (1999).
185. Dyer PE, Khosroshahi ME, and Tuft SJ. Studies of laser-induced cavitation and tissue ablation in saline using a fibre-delivered pulsed HF laser. *Appl. Phys. B*, 56:84–93 (1993).
186. Brinkmann R, Hansen C, Mohrenstecher D, Scheu M, and Birngruber R. Analysis of cavitation dynamics during pulsed laser tissue ablation by optical on-line monotoring. *IEEE J. Sel. Top. Quant. Electron.*, 2:826–835 (1996).
187. Frenz M, Könz F, Pratisto H, Weber HP, Silenok AS, and Konov VI. Starting mechanisms and dynamics of bubble formation induced by a Ho:Yttrium aluminium garnet laser in water. *J. Appl. Phys.*, 84:5905–5912 (1998).
188. Ith M, Pratisto H, Altermatt HJ, Frenz M, and Weber HP. Dynamics of laser-induced channel formation in water and influence of pulse duration on the ablation of biotissue under water with pulsed erbium-laser radiation. *Appl. Phys. B*, 59:621–629 (1994).
189. Vogel A, Engelhardt R, Behnle U, and Parlitz U. Minimization effects in pulsed laser ablation illustrated in laser angioplasty. *Appl. Phys. B*, 62:173–182 (1996).
190. Pratisto H, Frenz M, Ith M, Altermatt HJ, Jansen ED, and Weber HP. Combination of fiber-guided pulsed erbium and holmium laser radiation for tissue ablation under water. *Appl. Opt.*, 35:3328–3337 (1996).
191. Jansen ED, Asshauer T, Frenz M, Motamedi M, Delacrétaz G, and Welch AJ. Effect of pulse duration on bubble formation and laser-induced pressure waves during holmium laser ablation. *Lasers Surg. Med.*, 18:278–293 (1996).
192. Vogel A, Schmidt P, and Flucke B. Minimization of thermomechanical side effects in IR ablation by use of multiply Q-switched laser pulses. *Med. Laser Appl.*, 17:15–20 (2002).
193. Jansen ED, van Leeuwen TG, Motamedi M, Borst C, and Welch AJ. Partial vaporization model for pulsed mid-infrared laser ablation of water. *J. Appl. Phys.*, 78:564–571 (1995).
194. Skripov VP and Pavlov PA. Superheating and explosive boiling of liquids. *Sov. Tech. Rev. B. Therm. Phys.*, 2:171–207 (1989).
195. Skripov VP. Thermodynamic stabilities of superheated and supercooled liquids. *Fluid Mech. Res.*, 21:43–50 (1992).

196. Paltauf G, Schmidt-Kloiber H, and Frenz M. Photoacoustic waves excited in liquids by fiber-transmitted laser pulses. *J. Acoust. Soc. Am.*, 104:890–897 (1998).
197. Dingus RS. Laser-induced contained vaporization in tissue. *Proc SPIE*, 1646:266–274 (1992).
198. Vogel A, Noack J, Nahen K, Theisen D, Busch S, Parlitz U, Hammer DX, Noojin GD, Rockwell BA, and Birngruber R. Energy balance of optical breakdown in water at nanosecond to femtosecond time scales. *Appl. Phys. B*, 68:271–280 (1999).
199. van Leeuwen T G, Meertens JH, Velema E, Post MJ, and Borst C. Intraluminal vapor bubble induced by excimer laser pulse causes microsecond arterial dilitation and invagination leading to extensive wall damage in the rabbit. *Circulation*, 87:1258–1263 (1993).
200. Cross FW, Al-Dhahir RK, and Dyer PE. Ablative and acoustic response of pulsed UV laser-irradiated vascular tissue in a liquid environment. J. *Appl. Phys.*, 64:2194–2201 (1988).
201. Brujan EA, Nahen K, Schmidt P, and Vogel A. Dynamics of laser-induced cavitation bubbles near an elastic boundary. *J. Fluid Mech.*, 433:251–281 (2001).
202. Brujan EA, Nahen K, Schmidt P, and Vogel A. Dynamics of laser-induced cavitation bubbles near elastic boundaries: Influence of the elastic modulus. *J. Fluid Mech.*, 433:283–314 (2001).
203. Vogel A, Hentschel W, Holzfuss J, and Lauterborn W. Cavitation buble dynamics and acoustic transient generation in ocular surgery with pulsed neodymium:YAG lasers. *Ophthalmology*, 93:1259–1269 (1986).
204. Vogel A, Schweiger P, Frieser A, Asiyo M, and Birngruber R. Intraocular Nd:YAG laser surgery: Light-tissue interaction, damage range, and reduction of collateral effects. *IEEE J. Quant. Electron.*, 26:2240–2260 (1990).
205. Lin C, Stern D, and Puliafito CA. High-speed photography of Er.YAG laser ablation in fluid. *Invest. Ophthalmol. Vis. Sci.*, 31:2546–2550 (1990).
206. Vogel A, Busch S, and Parlitz U. Shock wave emission and cavitation bubble generation by picosecond and nanosecond optical breakdown in water. *J. Acoust. Soc. Am.*, 100:148–165 (1996).
207. Brennen CE. *Cavitation and bubble dynamics.* Oxford University, Oxford, New York (1995).
208. Vogel A, Lauterborn W, and Timm R. Optical and acoustic investigation of the dynamics of laser-produced cavitation bubbles near a solid boundary. *J. Fluid Mech.*, 206:299–338 (1989).
209. Palanker D, Vankov A, Miller J, Friedman M, and Strauss M. Prevention of tissue damage by water jet during cavitation. *J. Appl. Phys.*, 94:2654–2661 (2003).
210. Chapyak EJ and Godwin RP. Simulations of laser thrombolysis. *Proc. SPIE*, 3590:328–335 (1999).
211. Frenz M, Pratisto H, Könz F, Jansen ED, Welch AJ, and Weber HP. Comparison of the effects of absorption coefficient and pulse duration of 2.12 μm and 2.79 μm radiation on laser ablation of tissue. *IEEE J. Quant. Electron.*, 32:2025–2036 (1996).
212. Srinivasan R, Casey KG, and Haller JD. Subnanosecond probing of the ablation of soft plaque from arterial wall by 308 nm laser pulses delivered through a fiber. *IEEE J. Quant. Electron.*, 26:2279–2283 (1990).
213. Brinkmann R, Dröge G, Schröer F, Scheu M, and Birngruber R. Ablation dynamics in laser sclerostomy ab externo by means of pulsed lasers in the mid-infrared spectral range. *Ophthalm. Surg. Lasers*, 28:853–865 (1997).
214. Brinkmann R, Theisen D, Brendel T, and Birngruber R. Single pulse 30-J holmium laser for myocardial revascularisation – a study on ablation dynamics in comparison to CO_2 Laser. *IEEE J. Sel. Top. Quant. Electron.*, 5:969–980 (1999).
215. Jansen ED, van Leeuwen TG, Verdaasdonk RM, Le TH, Motamedi M, Welch AJ, and Borst C. Influence of tissue mechanical strength during UV and IR laser ablation in vitro. *Proc. SPIE*, 1882:139–146 (1993).
216. Frenz M, Mischler C, Romano V, Forrer M, Müller OM, and Weber HP. Effect of mechanical tissue properties on thermal damage in skin after IR-laser ablation. *Appl. Phys. B*, 52:251–258 (1991).

217. Jansen ED, Frenz M, Kadipasaoglu KA, Pfefer T, Altermatt HJ, Motamedi M, and Welch AJ. Laser-tissueinteraction during transmyocardial laser revascularisation. *Proc. SPIE*, 2671:49–57 (1996).
218. Müller G, Dörschel K, and Kar H. Biophysics of the photoablation process. *Lasers Med. Sci.*, 6:241–254 (1991).
219. Hibst R and Kaufmann R. Effects of laser parameters on pulsed Er-YAG laser skin ablation *Lasers Med. Sci.*, 6:391–397 (1991).
220. Schomacker KT, Walsh JT, Flotte TJ, and Deutsch TF. Thermal damage produced by high-irradiance continuous wave CO_2 laser cutting of tissue. *Lasers Surg. Med.*, 10:74–84 (1990).
221. Neev J, Da Silva LB, Feit MD, Perry MD, Rubenchik AM, and Stuart BC. Ultrashort pulse lasers for hard tissue ablation. *IEEE J. Sel. Top. Quant. Electron*., 2:790–800 (1996).
222. Majaron B, Srinivas SM, Huang HL, and Nelson JS. Deep coagulation of dermal collagen with repetitive Er:YAG laser irradiation. *Lasers Surg. Med.*, 26:215–222 (2000).